Endogenous electric field-driven neuro-immuno-regulatory scaffold for effective diabetic wound healing

Zhiqing Liu [a,1], Tianlong Wang [a,1], Jinhui Zhao [a,1], Lei Zhang [a,1], Yiping Luo [a], Yixing Chen [a], Xinhui Wu [a], Yaqi Liu [a], Aihemaitijiang Aierken [a], Dilixiati Duolikun [a], Hui Jiang [a], Xinyu Zhao [a], Chang Li [a], Yingchuan Li [e,**], Wentao Cao [d,***], Jianzhong Du [a,f,g,****], Longpo Zheng [a,b,c,*]

[a] Department of Orthopedics, Shanghai Tenth People's Hospital, School of Medicine, Tongji University, Shanghai, 200072, China
[b] Shanghai Trauma Emergency Center, Shanghai, 200072, China
[c] Orthopedic Intelligent Minimally Invasive Diagnosis & Treatment Center, Shanghai Tenth People's Hospital, School of Medicine, Tongji University, Shanghai, 200072, China
[d] Department of Prosthodontics, Shanghai Stomatological Hospital & School of Stomatology, Fudan University, Shanghai, 201102, China
[e] Department of Critical Care Medicine, School of Medicine, Shanghai Tenth People's Hospital, Tongji University, Shanghai, China
[f] Department of Polymeric Materials, School of Materials Science and Engineering, Tongji University, 4800 Caoan Road, Shanghai, 201804, China
[g] School of Materials Science and Engineering, East China University of Science and Technology, Shanghai, 200237, China

ARTICLE INFO

ABSTRACT

The pathological microenvironment in diabetic wounds is delineated by heightened inflammatory responses and persistent proinflammatory macrophage activity, which significantly hinders the wound healing process. Exogenous electrical stimulation (ES), by modulating the electric field distribution in wounds, has shown significant potential in treating inflammatory wounds. However, this approach relies on additional power sources and complex circuit designs. Here, a bionic neuro-immuno-regulatory (BNIR) system was proposed for reshaping the endogenous electric fields (EFs) through collecting ion flow. The BNIR system comprises microporous structure scaffolds and nanosheets, enabling swift biofluid collection and electrical signal transmission, with the ability to promote cell proliferation and migration and exhibit antioxidant properties. More importantly, the BNIR system induced the transition of M1 macrophages to M2 macrophages through neuro-immuno-regulatory. In diabetic rat skin wounds, the BNIR system significantly enhanced healing by simultaneously neuro-immuno-regulatory, promoting angiogenesis, scavenging ROS, and facilitating tissue remodeling. This work aims to advance the development of a bionic system for electrosensitive tissue repair.

1. Introduction

Given the continuous increase in the global morbidity rates associated with diabetes, it is estimated that the diabetic population will surpass the threshold of 500 million individuals by the year 2045 [1].

Diabetic patients exhibit susceptibility to the formation of chronic, non-healing wounds, constituting a formidable therapeutic challenge within clinical practice [2,3]. Chronic diabetic wound healing is hindered by impaired angiogenesis, elevated reactive oxygen species (ROS), and persistent excessive inflammation [4,5]. Excessive inflammation in

diabetic wounds hinders the transition from the inflammatory stage to the proliferative stage, with macrophages playing a crucial role as multifunctional regulator in this process [6–8]. Endogenous electric fields (EFs) are essential in the human body, influencing processes at cellular, tissue, and organ levels [9]. Extensive research has shown that electrical stimulation (ES) significantly enhances wound healing by reshaping EFs in diabetic wounds [10,11]. However, the widespread clinical adoption of ES-based wound dressings is constrained by the necessity for external devices to provide power and cause inconvenience for patients. Thus, developing functional materials that actively integrate EFs with wound healing is desirable.

The intricate healing of wounds comprises overlapping stages of hemostasis, inflammation, proliferation, and remodeling [12]. Among these stages, empirical studies unequivocally establish the pivotal role of EFs in wound healing [13]. The endogenous electric current effectively enhances both cell migration and proliferation [14]. Recent research has shown that a conductive hydrogel promotes the migration and proliferation of endothelial cells vital for angiogenesis by activating the PI3K/AKT and MEK/ERK pathways [15]. In addition, neural tissues are sensitive to electrical signals that regulate nerve cell behavior. The physiological activity of the neural network is regulated by EFs through feedback interactions [9]. More importantly, the interaction between the nervous and immune systems contributes to wound healing. Previous study indicated that harnessing neuro-immuno-regulatory holds promise for treating non-healing tissues [16]. The normal epidermis has a transepithelial potential due to uneven ion distribution. A wound causes current to flow from the injury, creating an electric field with the edge as anode, and the center as cathode [17]. Within injured tissues, ion flow dependent on the transport of wound exudate is a pivotal contributor to the generation of EFs, and the appropriate collection of exudate facilitates the transmission of endogenous electrical signals, thereby promoting tissue repair and reconstruction [18]. Moreover, wound exudate management holds a pivotal role in the construction of wound beds for chronic wounds, serving as the fundamental basis for promoting wound healing process [19]. Hence, developing biomaterials capable of early-stage secretion collection and proactive transmission of bioelectrical signals is crucial for the healing of diabetic wounds.

Hydrophilic materials offer a solution to the challenge of water absorption. Currently, various therapeutic approaches exist for promoting wound exudate, with hydrophilic dressings such as medical gauze, and natural polymers like gelatin, collagen protein, silk protein, etc [20]. Decellularized adipose tissue (DAT) is predominantly composed of densely arranged extracellular matrix (ECM) components including collagen I-VI [21]. Previous studies have indicated that the DAT is increasingly recognized as a promising option for soft tissue augmentation and reconstruction [22,23]. Moreover, the water absorption characteristics of materials are significantly influenced by both pore size and porosity. Recently, the freeze-forming technique has been employed to fabricate 3D sponge scaffolds to develop microporous structure [24]. Therefore, employing a freeze-forming technique may yield a scaffold capable of absorbing wound exudates and enhancing wound healing. Nevertheless, the DAT sponge scaffolds lack electroactivity, rendering them incapable of reacting to physiological electrical signals throughout the healing process. Inorganic nanomaterials are extensively employed to enhance electrical conductivity. Inorganic nanoparticles are easy to synthesize and functionalize, but their residual toxic accumulation poses a challenge to biocompatibility [25]. Recently, MXene nanosheets, particularly, have garnered considerable attention within the scientific community due to their unique combination of high conductivity, hydrophilicity, and favorable biocompatibility [26]. Moreover, ROS is a double-edged sword, and excessive levels can damage normal tissues and hinder wound healing. MXene nanosheets have been reported to exhibit intrinsic enzyme-like activities, effectively scavenging ROS including hydrogen peroxide (H_2O_2), hydroxyl radical ($\bullet OH$), and superoxide anion ($\bullet O_2-$) [27]. Therefore, MXene nanosheets not only enhance the conductivity of DAT scaffolds but also scavenge ROS,

improving the local wound microenvironment.

Here, inspired by the electrophysiological environment and structure of the skin tissue, a MXene-based DAT scaffold (a bionic neuro-immuno-regulatory system, BNIR system) was proposed for enhancing diabetic wound healing. In this study, the modification of MXene with polydopamine (PDA, pMXene) results in remarkable stability and antioxidative properties, while preserving its conductivity. The PDA coating effectively grafted the basic fibroblast growth factor (bFGF) by serving as an anchor. Furthermore, a freeze-forming technique was used to construct a 3D DAT sponge scaffold, aiming at handling wound exudate and hemostasis. pMXene@bFGF endows the 3D DAT sponge scaffold with conductivity, antioxidative properties, and the provision of bioactive factors. *In vitro*, the BNIR system not only exhibited favorable biocompatibility but also markedly enhanced cell proliferation, angiogenesis, and migration. The BNIR system induced the transition of M1 macrophages to M2 macrophages through neuro-immuno-regulatory. Moreover, the composite scaffold's potential to accelerate diabetic wound healing was systematically investigated using a diabetic rat model. Effective wound closure was achieved through the BNIR system, showing the therapeutic benefits of aggregating wound exudate, coupling of endogenous EFs, neuro-immuno-regulatory, scavenging ROS, and delivering bFGF in accelerating the healing of diabetic wounds. Finally, the BNIR system holds significant promise for regenerating other electrosensitive tissues including the heart, bone tissue, etc.

2. Results and discussion

2.1. Preparation and characterization of pMXene@bFGF

The preparation of pMXene@bFGF involved a series of key steps outlined in Fig. 1. These steps included the synthesis and modification of MXene and the loading of basic fibroblast growth factor (bFGF). First, the 2D Ti3C2 nanosheets were synthesized using a standard chemical exfoliation method, following the procedure described by Alhabeb et al. [28]. The synthesis process of MXene was illustrated in Fig. 2a. The transmission electron microscopy (TEM) images and the atomic force microscopy (AFM) images demonstrated the ultrathin morphology of MXene nanosheets (Figure S1 and Figure S2). Additionally, TEM images showed that the 2D layered structure of MXene@PDA was retained (Fig. 2b). The elemental mappings reveal a uniform distribution of C, N, O, and Ti. The signal from the N was uniformly distributed across the nanosheet, suggesting the uniform coating of polydopamine (PDA) on the MXene nanosheets (Fig. 2c). The Tyndall effect observed in MXene, and pMXene dispersions (Fig. S3) indicated that these are colloids below 100 nm in a certain dimension. Raman scattering was used to analyze the chemical groups in MXene and pMXene (Fig. S4). The D-peak (~1300 cm^{-1}) and G-peak (~1580 cm^{-1}) are Raman signatures of carbon crystals, reflecting lattice defects and in-plane sp^2-hybridized vibrations, respectively [29]. The range of 1580–1620 cm^{-1} is attributed to the stretching of carbon-carbon bonds [30]. The increased intensities of the D and G peaks in the Raman spectra of pMXene indicated a higher carbon content in the nanosheets.

The X-ray diffraction (XRD) patterns for Max, MXene, and pMXene were shown in Fig. 2d. The peak 002 of Ti3AlC2 exhibited a minor deviation towards a lower angle, and this observation can be linked to the partial substitution of the Al element with either hydroxyl or fluorine. The absence of peak 104 at 39° suggested a thorough and clean etching of the aluminum layer [4]. Moreover, the application of PDA coating on MXene maintained the peak position of MXene without any additional peak formation. This suggested that the amorphous phase of PDA was successfully loaded on the MXene. Subsequently, X-ray photoelectron spectroscopy (XPS) was employed for the analysis of the chemical composition of both MXene and pMXene. The distinctive peaks identified in the XPS spectrum of MXene provide conclusive insights into its elemental composition, including F, Ti, C, and O. The notable absence of
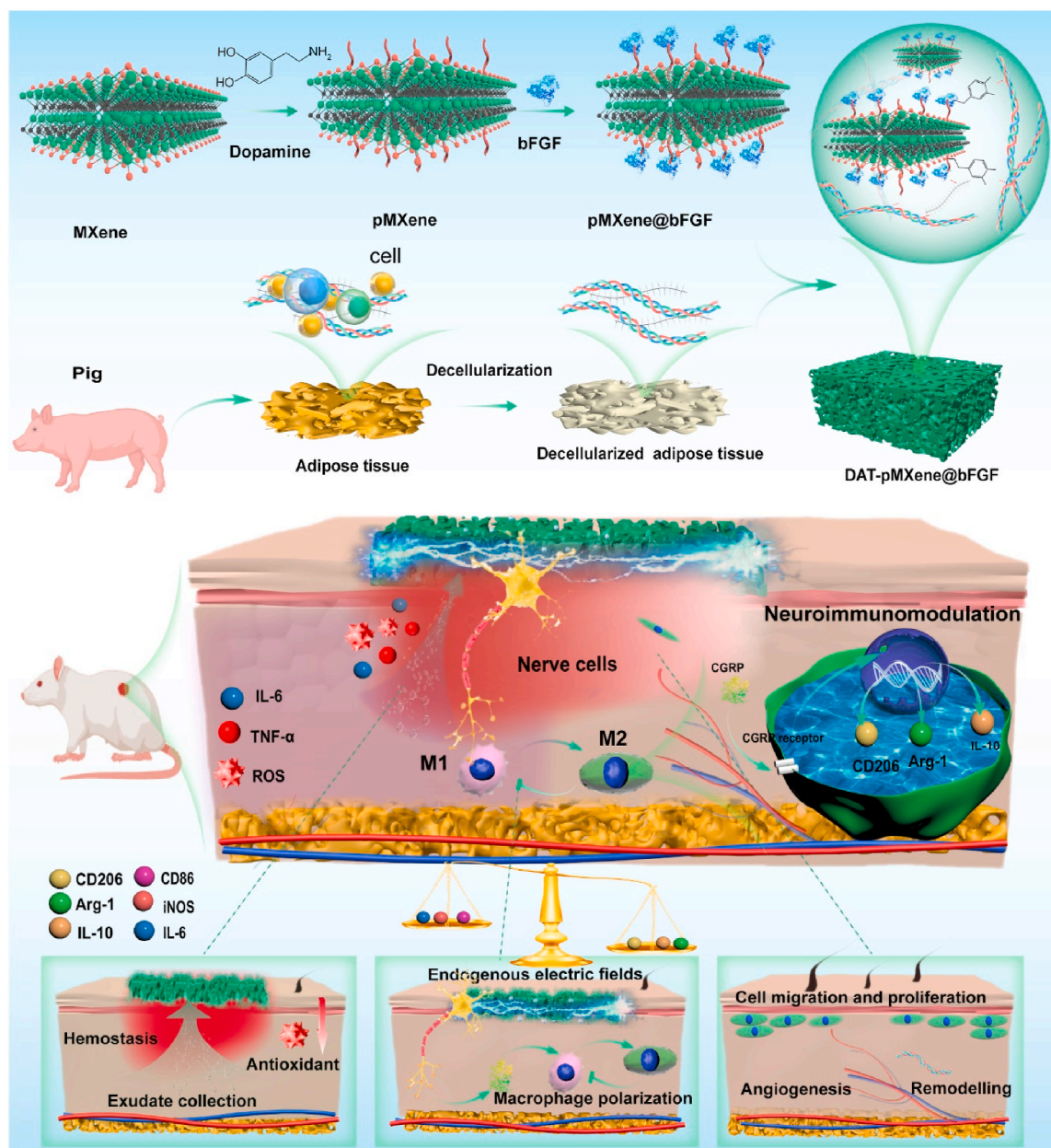
Fig. 1. Schematic illustrations of endogenous electric-field-driven neuro-immuno-regulatory through a conductive decellularized adipose tissue scaffold for diabetic wound healing.

Al within the spectrum serves as compelling evidence, confirming the efficacy of the etching process and substantiating the complete removal of the aluminum layer from the MAX substrate (Fig. S5). Moreover, the appearance of N 1s at 401.3 eV was ascribed to the binding of polydopamine (PDA), as depicted in Fig. S5.

bFGF, a mitogenic polypeptide, has been established to exert significant effects on skin regeneration [31,32]. The ultra-thin planar nanostructure in 2D bio-nanosystems offers a substantial surface area with numerous anchoring sites for therapeutic drug molecules [33]. MXene can serve as a drug delivery platform for bFGF. Zeta potentials analysis was used to evaluate the charge characteristics of the MXene, pMXene, bFGF, and pMXene@bFGF (Fig. S6). The pMXene showed a more pronounced negative charge value (-19.7 ± 1.3 mV) compared to MXene (-8.3 ± 1.2 mV), bFGF (-4.3 ± 0.7 mV), and pMXene@bFGF (-10.9 ± 1.7 mV). Moreover, the UV–vis absorption spectra of MXene, PDA, bFGF, and pMXene@bFGF were detected. Changes in the characteristic peaks of the UV absorption spectrum indicated the successful

loading of bFGF onto pMXene (Fig. S7). Furthermore, the loading efficiency of bFGF was 60.4 %. The release of bFGF exhibited an initial burst during the first two days, followed by a slower and sustained release over the subsequent days (Fig. S8).

2.2. Characterization of DAT-pMXene@bFGF scaffolds

Histological analysis demonstrated the successful preparation of a decellularized extracellular matrix. The absence of cells was conclusively ascertained through rigorous histological examination employing H&E staining, Masson's Trichrome staining, Oil red O staining, and DAPI staining (Fig. S9). Furthermore, Masson's Trichrome staining was utilized for a more in-depth analysis of collagen. The microstructural characteristics of DAT, DAT-pMXene, and DAT-pMXene@bFGF scaffolds were assessed using scanning electron microscopy (SEM) (Fig. 2e and Figure S10, S11). The SEM depicted uniformly distributed and interconnected porous microstructures in all types of scaffolds. Elemental
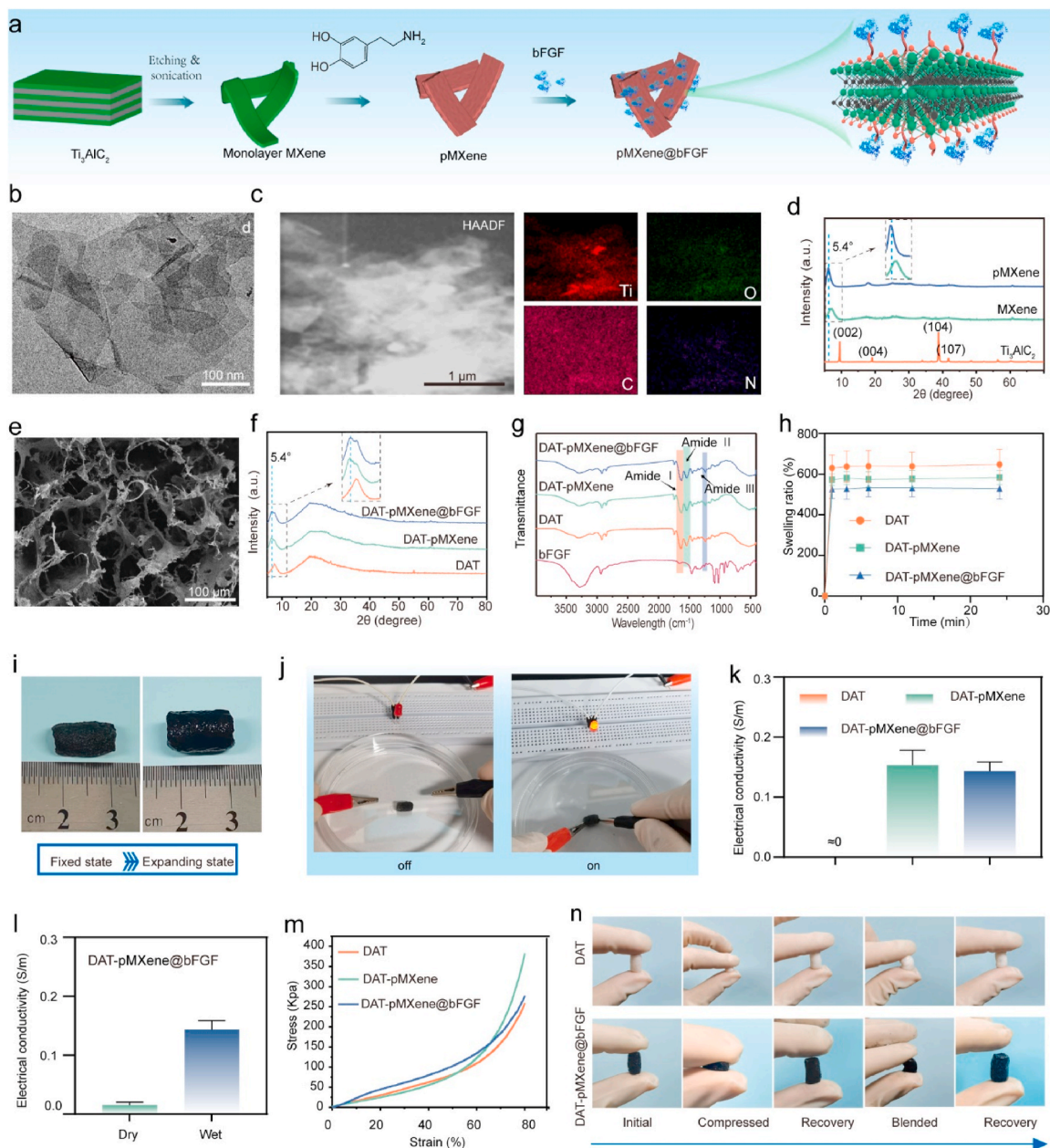
Fig. 2. Preparation and characterization of DAT-pMXene@bFGF scaffolds. (a) Schematic illustration of the synthesis of pMXene nanosheets. (b) TEM image of pMXene nanosheets. (c) Elemental mapping images of pMXene nanosheets. (d) XRD patterns of MAX, MXene, and pMXene. (e) SEM image of DAT-pMXene@bFGF scaffolds. (f) XRD patterns of DAT, DAT-pMXene, and DAT-pMXene@bFGF. (g) FTIR spectra of bFGF DAT, DAT-pMXene, and DAT-pMXene@bFGF. (h) Swelling ratio of DAT, DAT-pMXene, and DAT-pMXene@bFGF. (i) Expanding condition of pMXene nanosheets following water absorption. (j) The LED was illuminated in wet conditions by the DAT-pMXene@bFGF-integrated circuit. (k) The electrical conductivity of DAT, DAT-pMXene, and DAT-pMXene@bFGF (n = 3). (l)The electrical conductivity of DAT-pMXene@bFGF was observed in both wet and dry states (n = 3). (m) Compressive stress-stain curves of DAT, DAT-pMXene, and DAT-pMXene@bFGF. (n) Photographs of the compression and bending resistance of DAT, and DAT-pMXene@bFGF.

mapping through Energy Dispersive Spectroscopy (EDS) (Figs. S12 and S13) confirmed the uniform distribution of Ti, C, O, and N within the DAT-pMXene@bFGF scaffolds. Furthermore, the XRD results exhibited the characteristic MXene peaks within the DAT-pMXene@bFGF scaffolds, indicating the successful integration of pMXene@bFGF (Fig. 2f). Additionally, according to the thermogravimetric analysis (TGA) results of DAT, DAT-pMXene, and DAT-pMXene@bFGF (Fig. S14). At 800 °C, the residual mass of DAT-pMXene (6.0 %) and DAT-pMXene@bFGF (5.7 %) was slightly higher than that of DAT (3.3 %).

As shown in Fig. 2g, Fourier Transform infrared spectroscopy (FTIR) spectra displayed characteristic peaks denoting amide I, II, and III at 1630, 1546, and 1236 cm^{-1}, respectively. The characteristic peak of

MXene and bFGF did not appear distinct in the DAT-pMXene, and DAT-pMXene@bFGF spectra, potentially obscured by the overlapping DAT spectra.

The scaffold's exceptional water absorption plays a crucial role in supporting tissue regeneration, primarily by effectively collecting surplus biofluid from wounds and minimizing the risk of infection [19]. Additionally, the absorption of wound exudates aids in ion flow, thereby enhancing the transmission of electrical signals. Here, the hygroscopic properties of these scaffolds were evaluated by examining their water absorption both before and after modification. Fig. 2h illustrated the water absorption properties of DAT, DAT-pMXene, and DAT-pMXene@bFGF scaffolds, all of which reach peak absorption and

swelling within a short period. The DAT-pMXene@bFGF scaffolds exhibited swift water absorption upon soaking (Fig. 2i). The superior water absorption performance of these scaffolds can be attributed to their interconnected porous structure, which facilitates effective water absorption and retention. The quantitative assessment of porosity revealed that the incorporation of nanosheet layers did not significantly affect the porosity of the DAT scaffolds (Fig. S15).

The mechanical stability of scaffolds ensured reversible water absorption. DAT, DAT-pMXene, and DAT-pMXene@bFGF scaffolds exhibited similar mechanical properties (Fig. 2m and Fig. S16). Moreover, DAT-pMXene@bFGF scaffolds, similar to DAT scaffolds, displayed elasticity, nearly returning to their initial cylindrical shape after the external compression (Fig. 2n). The initial phase of wound healing involves achieving rapid and effective hemostasis. SEM images revealed that compared to gauze and DAT, the surfaces of DAT-pMXene@bFGF had a higher adhesion of red blood cells. (Fig. S17). Moreover, the hemostatic capability of the scaffolds was further investigated in a rat liver injury model (Fig. S18). It was observed that DAT-pMXene@bFGF was effective in reducing bleeding.

Conductive dressings were known to facilitate wound healing [34]. The electrical conductive properties of the scaffolds were depicted in Fig. 2j and k. An illuminated light-emitting diode (LED) was observed, especially within a scaffold-connected circuit that contained pMXene@bFGF nanosheets. The DAT-pMXene and DAT-pMXene@bFGF scaffolds demonstrated a substantial increase in conductivity when compared to the negligible conductivity observed in pure DAT scaffolds. Furthermore, the DAT-pMXene@bFGF scaffolds exhibited a conductivity of 0.14 ± 0.02 S/m in the wet state (Fig. 2l). Normal skin tissue has a conductivity of 10^{-7} to 2.6×10^{-3} S/cm, and electroactive dressings with similar conductivity can promote wound healing [35,36]. Thus, the conductive scaffolds, exhibiting conductivity similar to that of skin, are anticipated to enhance wound healing.

The degradation properties are critically important for tissue repair and regeneration [37]. The degradation profiles of the DAT, DAT-pMXene, and DAT-pMXene@bFGF were recorded (Fig. S19). The slower degradation rate in the DAT-pMXene and DAT-pMXene@bFGF groups is likely due to the presence of pMXene. Additionally, during the degradation process, both the electrical conductivity and antioxidant properties of DAT-pMXene@bFGF exhibited a slight decline (Fig. S19).

2.3. In vitro effects of the composite scaffolds

In clinical applications for wound dressings, the composite scaffolds must exhibit favorable biocompatibility as a fundamental requirement. In this study, both HUVECs and NIH-3T3 were employed to assess the effect of composite scaffolds on cell viability and proliferation *via* live/dead staining, phalloidin staining, and CCK-8 assay. First, the cytotoxicity of DAT-pMXene@bFGF scaffolds was further analyzed using live/dead cell staining. After 1 day of cultivation, HUVECs and NIH-3T3 cells were stained with live/dead cell kits. Live/Dead staining (Fig. 3a) demonstrated the satisfactory biocompatibility of DAT-pMXene@bFGF scaffolds overall. Subsequently, after culturing HUVECs and NIH-3T3 cells separately with the scaffolds, cytoskeleton staining and SEM were performed on day 1. The main objective was to evaluate the morphology of HUVECs and NIH-3T3, which are essential factors for the foundation of skin wound healing. The images validated the favorable cell adhesion and spreading behaviors on the DAT-pMXene@bFGF scaffolds (Fig. 3a and Fig. S20). Furthermore, the CCK-8 findings and Live/Dead staining additionally verified cell proliferation across all groups, with significantly higher cell numbers in DAT-pMXene@bFGF after 5 days compared to other groups ($P < 0.05$) (Fig. 3b, c and Fig. S21). Moreover, the hemolysis assay was employed to assess the blood compatibility of the composite scaffolds, as the hemolytic rate (HR) is a crucial indicator for evaluating biomaterial compatibility [31]. As illustrated in Fig. 3d, the composite scaffolds exhibited notable hemocompatibility, with the

hemolysis rates all below 5 %. In summary, the DAT-pMXene@bFGF scaffolds exhibited biocompatibility, non-hemolytic properties, and promoted cell adhesion, growth, and proliferation.

2.4. Angiogenesis, and cell migration

A tube formation assay was performed to assess the impact of DAT-pMXene@bFGF on the angiogenic potential of HUVECs. In comparison to the control groups, the DAT-pMXene@bFGF group displayed the most robust development of tubular networks after 4 h of incubation (Fig. 3e–g). Furthermore, the migratory potentials of NIH-3T3 and HUVECs cells were pivotal for the process of vascularization [38]. Migration assay and scratch assay were selected as the assessment modalities for the composite scaffolds. Implementing the cell migration assay using a transwell system involved situating NIH-3T3 and HUVECs in the upper chamber and placing the composite scaffolds in the lower chamber. The DAT-pMXene@bFGF group exhibited a notably higher number of migrated cells compared to other groups, which suggested that the DAT-pMXene@bFGF group has the potential to enhance the homing of NIH-3T3 and HUVECs to the wound (Fig. 3h–j). Moreover, a scratch assay has been employed to explore further the migratory capacity of HUVECs cultured with the composite scaffolds. In Fig. S22, it is evident that the DAT-pMXene@bFGF group significantly facilitated HUVEC migration and the closure of cell-free gaps, demonstrating a superior performance compared to the control, DAT, and DAT-pMXene groups.

2.5. The antioxidative capability of DAT-pMXene@bFGF

Growing evidence indicates that elevated oxidative stress plays a crucial role in the pathogenesis of compromised diabetic wound healing [39]. MXene nanosheets can effectively scavenge a variety of ROS, including hydrogen peroxide (H_2O_2), hydroxyl radical ($\bullet OH$), and superoxide anion ($\bullet O_2-$), offering non-enzymatic antioxidant properties to mitigate oxidative stress-induced damage [40]. The antioxidative properties of the scaffolds were evaluated using 2, 2-diphenyl-1-picrylhydrazyl radical (DPPH) and 2,2′-azino-bis(3-ethyl-benzthiazoline-6-sulfonic acid) radical ion (ABTS) free radical scavenging assay. In ethanol, DPPH, a stable free radical, shows a purple color with a reliable absorption peak at 517 nm, serving as an indicator for monitoring the reduction [41]. As shown in Fig. 4a and Fig. S23a, the DAT-pMXene, and DAT-pMXene@bFGF groups exhibited a superior scavenging ratio compared to the control, and DAT groups, indicating the effects of pMXene in contributing to the DPPH scavenging activity. Moreover, the oxidation of ABTS produced $ABTS^{\bullet+}$, yielding a vibrant blue-green solution with a distinctive absorption peak at 734 nm [42]. As depicted in Fig. 4b and Fig. S23b, the results affirmed the DAT-pMXene and DAT-pMXene@bFGF's effective capacity for ABTS scavenging. Moreover, the removal of $\bullet OH$, $\bullet O_2-$, and H_2O_2 were monitored using electron spin resonance (ESR) spectroscopy. The ESR signals of the characteristic peaks for $\bullet OH$, $\bullet O_2-$, and H_2O_2, significantly reduced on the addition of DAT-pMXene@bFGF (Fig. S24). Elevated ROS levels characterize diabetic wounds, indicating a persistent state of oxidative stress [39]. DAT-pMXene@bFGF possesses the capability to shield cells from ROS-induced damage, attributed to their effective antioxidative activity as validated by cellular ROS scavenging experiments (Fig. 4c). H_2O_2 was employed to stimulate the generation of ROS within cells. Subsequently, the intracellular ROS scavenging efficacy of the composite scaffolds was further investigated through the utilization of the 2,7-dichlorodihydrofluorescein diacetate (DCFH-DA) probe. As shown in Fig. 4d–g, a robust green fluorescence signal was detected in the control group following the introduction of H_2O_2, indicating elevated levels of ROS. In addition, the DAT-pMXene@bFGF scaffolds were capable of significantly reducing intracellular (NIH-3T3 and HUVECs) levels of ROS (Fig. 4e–h). Increased levels of ROS induce oxidative stress and disrupt mitochondrial function, ultimately
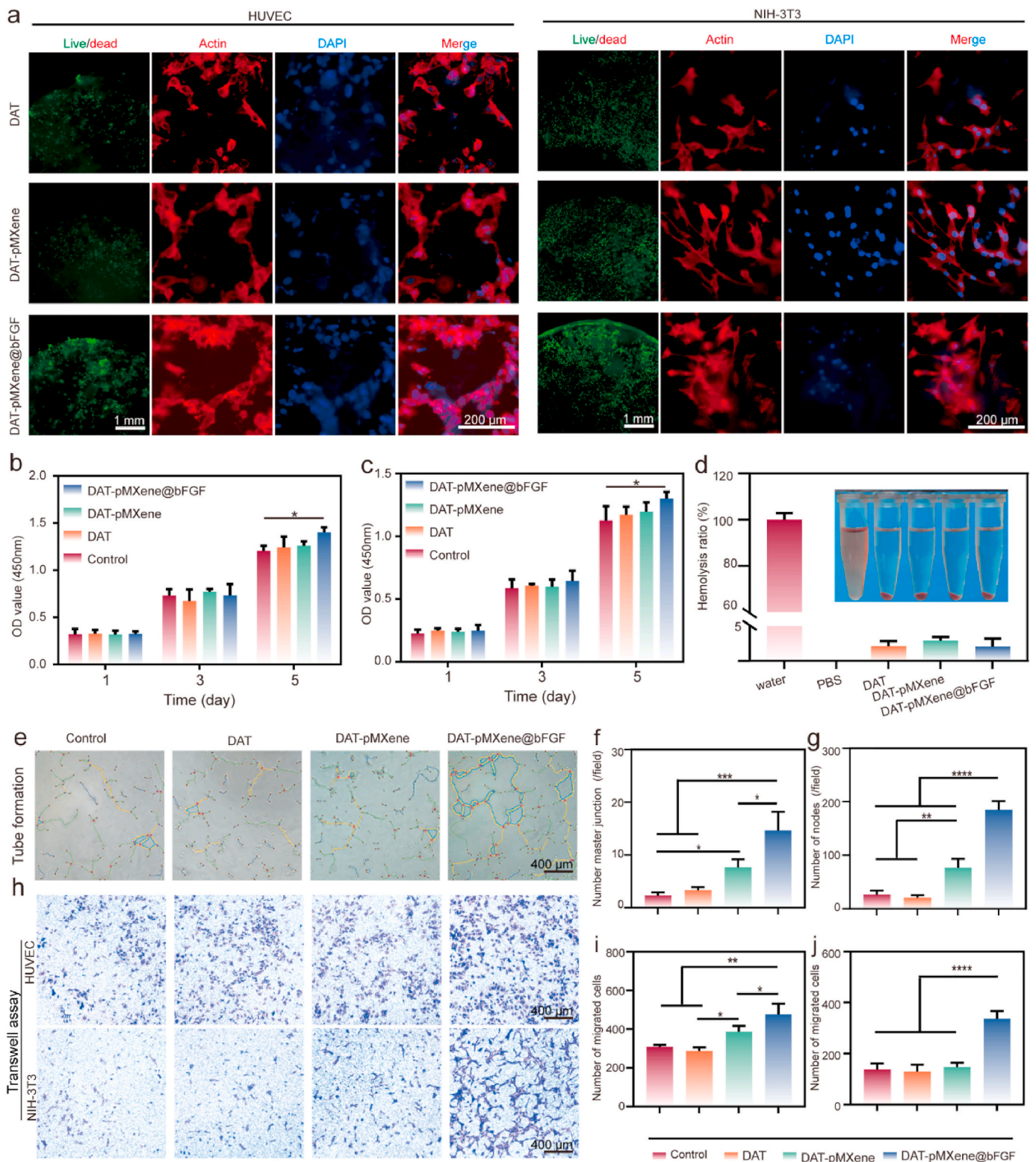
Fig. 3. Effects of composite scaffolds on cell viability, proliferation, migration, and tube formation. (a) Living/dead staining, and immunofluorescence staining images of HUVECs, and NIH-3T3 cells on composite scaffolds. Proliferation of (b) HUVECs, and (c) NIH-3T3 cells with CCK-8 for 1, 3, and 5 days (n = 3). (d) Hemolysis test of composite scaffolds (n = 3). (e–g) Tube formation assay by coculturing HUVECs with composite scaffolds (n = 3). (h) Crystal violet staining of HUVECs, and NIH-3T3 cells in transwell co-culture system. Quantification of (i–j) HUVECs, and NIH-3T3 migration (n = 3). Significance levels were denoted as $*P < 0.05$, $**P < 0.01$, $***P < 0.001$, and $****P < 0.0001$, to indicate statistical significance.
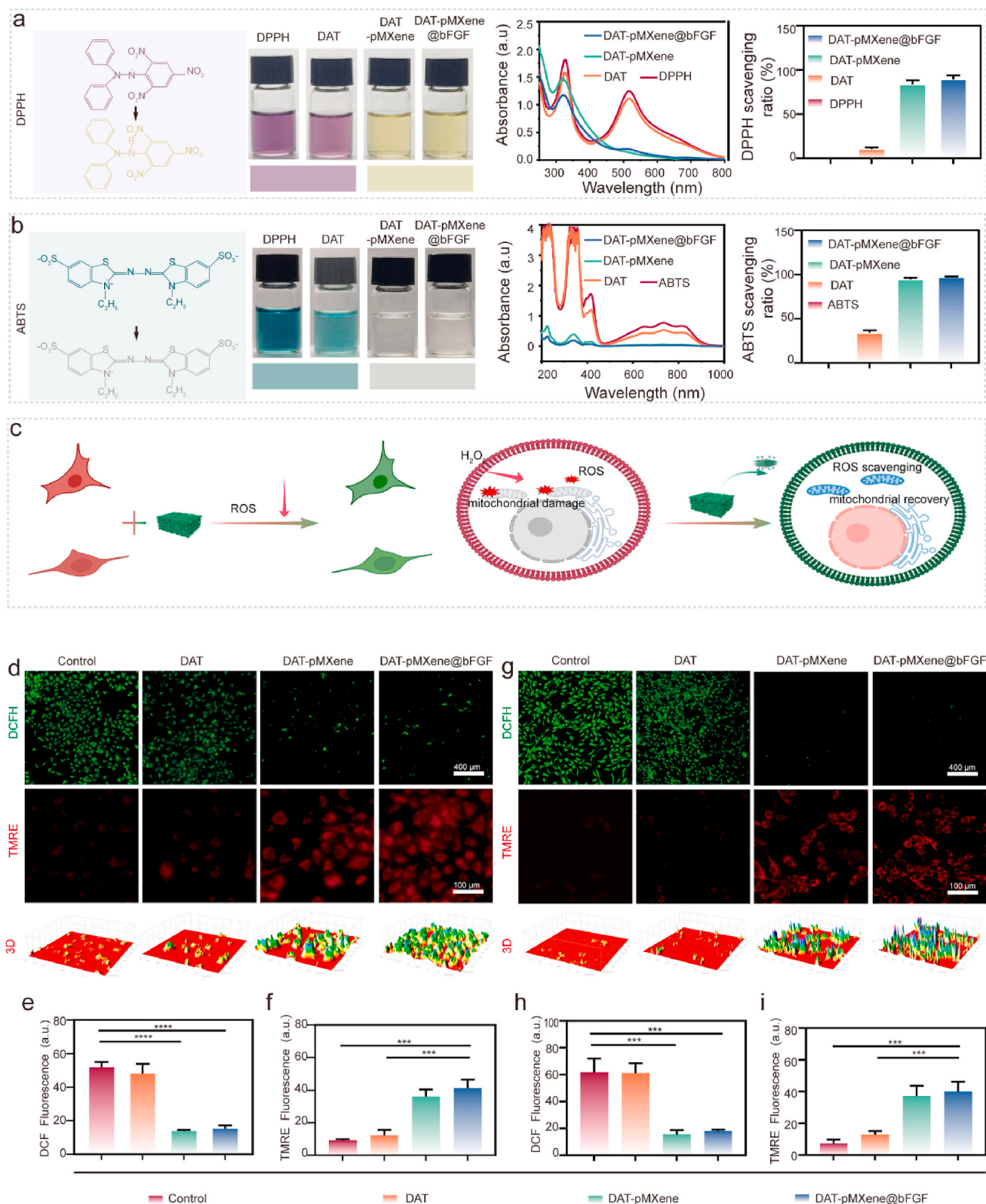
Fig. 4. *In vitro* evaluation of the antioxidant properties of composite scaffolds. (a, b) The mechanism, absorbance profiles, and scavenging capacity of composite scaffolds against two different free radicals: (a) DPPH, (b) ABTS (n = 3). (c) Illustration outlining the cytoprotective influence of composite scaffolds, achieved through the alleviation of oxidative damage induced by ROS. Fluorescence images showing the intracellular ROS, mitochondrial membrane potential detection, and 3D surface plot images (TMRE) in (d) HUVECs, and (g) NIH-3T3 cells stimulated with H_2O_2, co-cultured with composite scaffolds. (e–i) Quantification of intracellular ROS, and mitochondrial membrane potential in HUVECs, and NIH-3T3 cells: (e, f) HUVECs, (h, i) NIH-3T3 (n = 3). Significance levels were denoted as $*P < 0.05$, $**P < 0.01$, $***P < 0.001$, and $****P < 0.0001$, to indicate statistical significance.

culminating in irreversible cell death [43]. Proper mitochondrial function is commonly assessed through the reliable marker of mitochondrial membrane potential (ΔΨm). In this study, mitochondrial functions were assessed using TMRE (tetramethylrhodamine, ethyl ester) fluorescent staining. As shown in Fig. 4d–f, g, and i, the DAT-pMXene@bFGF group demonstrated robust red fluorescence, contrasting with minimal red fluorescence in the control and DAT groups, suggestive of the DAT-pMXene@bFGF scaffold's potentials in reinstating mitochondrial membrane potential. In summary, these results suggested that DAT-pMXene@bFGF exhibits the capacity to mitigate H_2O_2-induced intracellular ROS levels, maintaining a lowered ROS environment and promoting improved cell survival amidst oxidative stress.

2.6. DAT-pMXene@bFGF scaffolds promote macrophage polarization through nerve cells in vitro

Cell behaviors, such as adhesion, proliferation, self-renewal, differentiation, and cellular signaling, can be influenced by conductive biomaterials [44]. Electrical properties are crucial for nerve tissue engineering as they facilitate bioelectrical signal transmission [9]. Hence, the influence of the conductive DAT-pMXene@bFGF scaffolds on neuronal cells was investigated *in vitro* (Fig. 5a). After 1 day of cultivation, Schwann cells (SCs) were stained with a live/dead cell kit. Live/dead cell staining performed on day 1 post-seeding indicated substantial cell survival in different groups (Fig. 5b). In addition, SCs were assessed using S100-β and GFAP immunofluorescence staining. In SCs, GFAP supports injury response and repair, while S100-β promotes proliferation, differentiation, and nerve regeneration, aiding nerve repair [45]. The results indicated that S100-β and GFAP expression were significantly higher in the DAT-pMXene and DAT-pMXene@bFGF groups compared to the control and DAT groups (Fig. 5c and d), suggesting that the conductive DAT-pMXene@bFGF scaffolds enhanced the expression of SCs-related functional proteins. Furthermore, the process length of SCs in the DAT-pMXene and DAT-pMXene@bFGF scaffolds groups was significantly longer than in the control and DAT groups, indicating that DAT-pMXene@bFGF scaffolds promote outgrowth of SCs. Transwell assays (Fig. 4e–g) showed a significant increase in the number of migrating macrophages in the DAT-pMXene@bFGF + SCs group compared to other groups, indicating that DAT-pMXene may boost SCs' ability for macrophage recruitment. Macrophages, as integral constituents of the immune system, are centrally involved in safeguarding the host through essential contributions to defense mechanisms, wound-healing processes, and the regulation of immune responses [46]. In diabetic pathological wounds, macrophages demonstrated impaired transition from the pro-inflammatory M1 phenotype to the anti-inflammatory M2 phenotype, thereby prolonging inflammation, impeding angiogenesis, and delaying wound healing [12]. Research indicated that harnessing neuro-immuno-regulatory may address non-healing tissues where dysregulation impairs repair [16]. In this study, DAT-pMXene@bFGF was utilized in a co-culture system of SCs and RAW264.7 cells to investigate the potential to regulate the communication between the cell types. The grouping arrangement is depicted in Fig. 5h. To assess macrophage polarization, immunofluorescence staining was employed to detect CD206 (M2 marker) and CD86 (M1 marker) under inflammatory conditions. In the DAT-pMXene@bFGF + SCs group, there was an observed augmentation in CD206 staining with a reduction in CD86 staining compared to the control, SCs, and DAT-pMXene@bFGF groups, indicating an enhanced M2 activation (Fig. 5i and j). Moreover, flow cytometry was employed to detect macrophage transformation levels in different groups, revealing that after LPS stimulation, the DAT-pMXene@bFGF + SCs group displayed a proportion of 27.8 % CD86$^+$ (M1) macrophages and 24.5 % CD206$^+$ (M2) and (Fig. 5k and l). These results indicated that DAT-pMXene@bFGF induce the transition of M1 macrophages to M2 macrophages through the communication between SCs and RAW264.7 cells. Previous study suggested that CCL2 secretion by SCs is linked to

the regulation of macrophage polarization towards M2. SCs communicate with macrophages, promoting M2 macrophage polarization by inhibiting the nuclear factor-κB (NF-κB) pathway and enhancing antioxidant effects through cytokine regulation, thereby improving the microenvironment [47]. Moreover, the levels of NF-κB signaling pathway and cytokines in macrophages play a critical role in wound healing [48].

To elucidate the mechanism by which DAT-pMXene@bFGF with SCs promotes M2 macrophage polarization, we examined NF-κB signaling pathways, and various cytokines (iNOS, TNF-α, and IL-10). We found that DAT-pMXene@bFGF combined with SCs can inhibit the NF-κB pathway, suppress iNOS, and TNF-α secretion, and increase IL-10 expression (Fig. 5m). Thus, DAT-pMXene@bFGF combined with SCs can communicate with macrophages to block the NF-κB pathway, regulate cytokine levels, and alleviate the inflammatory state. For the evaluation of anti-inflammatory effects, qPCR analysis was conducted to detect the expression of genes associated with inflammatory regulation in macrophages, as shown in Fig. 5n. The findings revealed that DAT-pMXene@bFGF through nerve cells downregulated mRNA expression levels of iNOS, IL-6, and upregulated Arg-1, IL-10.

2.7. Evaluation of diabetic wound healing

Initially, a rat diabetes model was established *via* continuous tail intravenous administration of streptozotocin (STZ). Subsequently, a full-thickness diabetic wound model was created to investigate the effect of DAT-pMXene@bFGF on *in vivo* diabetic wound healing (Fig. 6a). Photographs were taken on days 0, 3, 7, and 14 to monitor the progress of wound healing (Fig. 6b). As shown in Fig. 6c, the photographs of wounds in distinct groups revealed significant variations on days 0, 3, 7, and 14. Furthermore, based on photographs of the wound and the quantitative analysis (Fig. 6d), it was observed that the wound size in the DAT-pMXene and DAT-pMXene@bFGF groups reduced at a faster rate compared to the control and DAT groups. Over the 14 days, the wounds treated with DAT-pMXene@bFGF consistently exhibited the most favorable condition, achieving a healing percentage of 96.9 ± 0.8 %. In comparison, the healing percentages for the control, DAT, and DAT-pMXene groups are 69.3 ± 2.7 %, 74.8 ± 2.7 %, and 82.1 ± 2.8 %, respectively.

Re-epithelialization was identified as the primary step in the healing of the dermis, preceding the overall process of skin wound repair [49]. H&E staining was carried out on days 7, and 14 to examine the re-filling of wound beds and the re-epithelialization process. The results verified that re-epithelialization in the DAT-pMXene@bFGF group during the remodeling phase, while the control group experienced delayed wound healing (Fig. 6e, Fig. S25). Specifically, after 14 days of treatment, wounds in the DAT-pMXene@bFGF group displayed almost complete healing and showcased a histological structure closely resembling that of normal rat skin. Moreover, H&E staining of major organs (heart, lung, liver, spleen, and kidney) revealed normal tissue structure in the DAT-pMXene@bFGF group (Fig. S27).

The process of wound healing is modular, encompassing three phases that overlap but maintain distinct characteristics: inflammation, proliferation, and remodeling [50]. The difficulty in healing chronic wounds is primarily attributed to the enduring presence of inflammatory wound environments [51]. It is consistently distinguished by neutrophil infiltration and an increased concentration of proinflammatory cytokines. First, the immunohistochemistry of tumor necrosis factor (TNF-α) and Interleukin-6 (IL-6) were carried out. As shown in Fig. 7a and b and Fig. S26, in comparison to the control and DAT groups, the DAT-pMXene and DAT-pMXene@bFGF groups exhibited decreased TNF-α and IL-6 signals around the central injury area. Moreover, in contrast to DAT-pMXene, DAT-pMXene@bFGF exhibited enhanced anti-inflammatory efficacy. During the proliferation phase, neovascularization is imperative for facilitating nutrient and oxygen transportation to the wound, thereby supporting fibroblast proliferation,
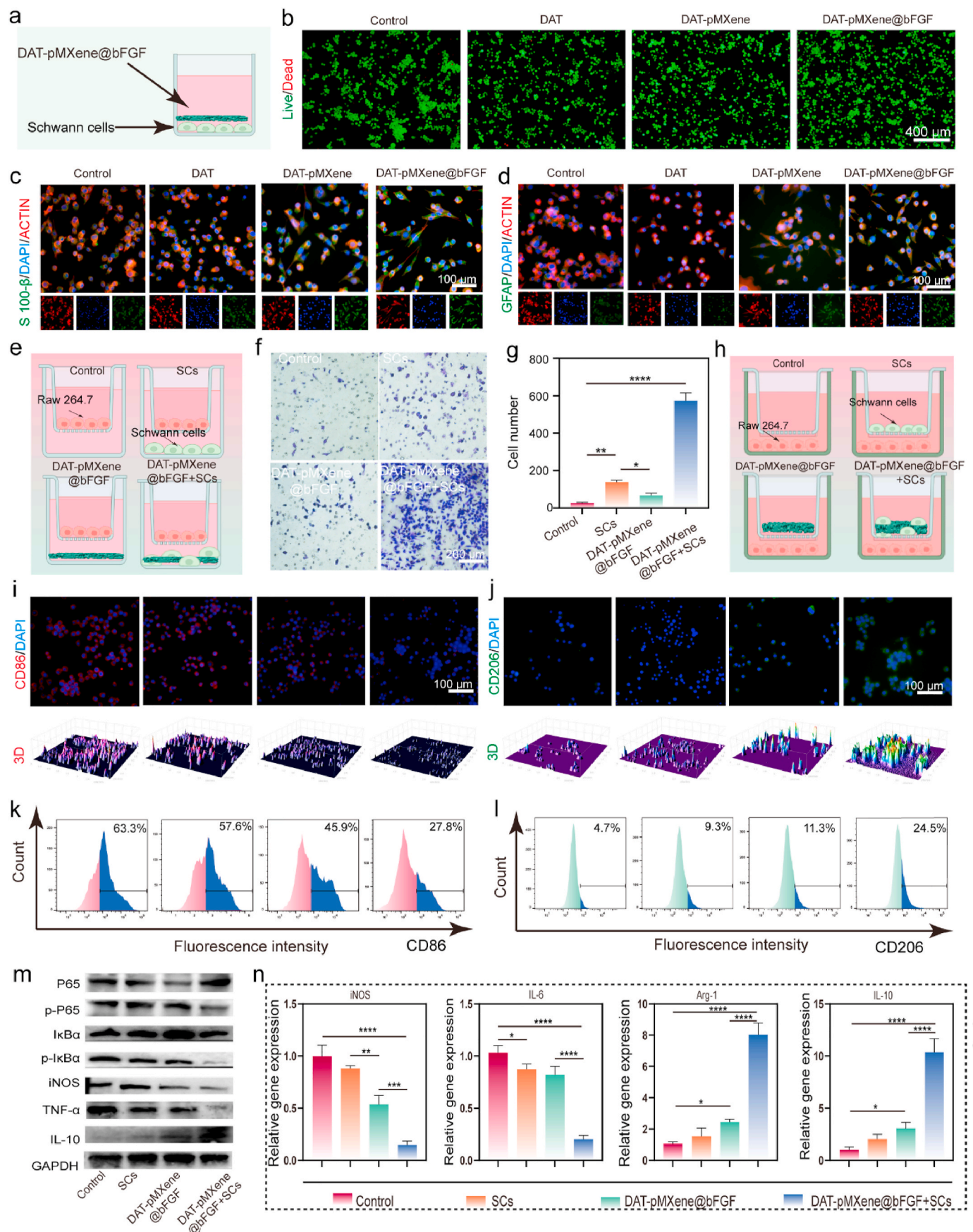
Fig. 5. DAT-pMXene@bFGF scaffolds promote macrophage polarization through nerve cells *in vitro*. (a) Illustration of cell-scaffolds co-culture model. (b) Living/dead staining of SCs. (c) S-100β immunofluorescence staining of SCs. (d) GFAP immunofluorescence staining of SCs. (e) Illustration of SCs with DAT-pMXene@bFGF scaffolds promoting migration of RAW264.7. (f) Images of RAW264.7 migration in a 24-h co-culture transwell system. (g) Quantification of RAW264.7 migration (n = 3). (h) Illustration of the method used to culture RAW264.7. (i) Immunofluorescence staining of CD86 and 3D surface plot images. (j) Immunofluorescence staining of CD206 and 3D surface plot images. (k, l) Flow cytometric evaluation of RAW264.7 cell expression levels for CD86 (M1) and CD206 (M2). (m) The expression levels of related proteins in RAW264.7 cells. (n) qPCR analysis to quantify the relative expression levels of M1-associated genes (iNOS, IL-6) and M2-related genes (Arg-1, IL-10) (n = 3). Significance levels were denoted as *$P < 0.05$, **$P < 0.01$, ***$P < 0.001$, and ****$P < 0.0001$, to indicate statistical significance.

collagen synthesis, and re-epithelialization. Immunofluorescence of α-SMA and CD31 was performed on day 7 to precisely identify the localization of neovascularization. On day 7, the wound sections treated with DAT-pMXene and DAT-pMXene@bFGF showed higher levels of α-SMA and CD31 compared to the control and DAT groups, with DAT-pMXene@bFGF displaying the highest expression levels (Fig. 7c, d and Fig. S26). Collagen serves as a crucial component of the extracellular matrix, playing a key role in the healing process and the restoration of skin strength [52]. Consequently, Masson's trichrome staining was carried out to observe the newly generated collagen. These results (Fig. 7e) revealed that, after 14 days, the density of collagen fibers in the wound bed was notably elevated in the DAT-pMXene@bFGF group compared to other groups, indicating a significant increase in the deposition of the extracellular matrix (DAT) in wounds treated with DAT-pMXene@bFGF.

Moreover, the excessive production of ROS is a consequence of the over-activation of inflammatory responses. For the evaluation of *in vivo* ROS scavenging capability, a dihydroethidium (DHE) probe was employed to assess the ROS content in the wound bed. In Fig. 7f and g, the red fluorescence intensity in the DAT-pMXene@bFGF group was notably reduced compared to the control group, indicating remarkable *in vivo* ROS scavenging and antioxidative efficacy. *In vitro*, it was demonstrated that the DAT-pMXene@bFGF induces the transition of M1 macrophages to M2 macrophages through the communication between SCs and RAW264.7 cells. In addition, nociceptor endings extend into injured skin during the healing process, signaling to immune cells *via* the neuropeptide calcitonin gene-related peptide. As shown in Fig. 7h and i, DAT-pMXene and DAT-pMXene@bFGF treatment significantly increased calcitonin gene-related peptide expression compared to the other groups, with no significant difference between the DAT and control groups. To confirm the ratio between M2 macrophages (Arg-1) and M1 macrophages (iNOS), double immunofluorescence staining was carried out, as shown in Fig. 7j. In comparison to the control, DAT-pMXene, and DAT Groups, the DAT-pMXene@bFGF group markedly reduced the count of pro-inflammatory M1 macrophages and concurrently increased the formation of anti-inflammatory M2 macrophages (Fig. 7k and l). Hence, our study indicated that DAT-pMXene@bFGF has the potential to enhance endogenous electric-field-driven neuro-immunomodulation, thereby facilitating the transition of macrophage polarization from the M1 phenotype to the M2 phenotype.

Certainly, this study has some limitations. It utilized H_2O_2 to simulate oxidative stress in a diabetic wound cell model, but did not fully replicate the hyperglycemic conditions typical of diabetic environments. Future cell-based studies should incorporate high-glucose conditions to better mimic the pathophysiology of diabetic wound healing. In a diabetic rat model, the BNIR system accelerated wound healing by aggregating wound exudate, enhancing endogenous EF, modulating neuro-immune responses, scavenging ROS, and delivering bFGF. The scaffold material utilized in the BNIR system is DAT. DAT shows promise in regenerative medicine, though some challenges remain in its clinical translation. Ensuring consistency in the decellularization process to maintain quality and minimize immune responses, along with addressing variability in raw materials and production scalability, are important considerations. Efforts in optimizing processes, controlling costs, and navigating regulatory requirements will further support the clinical application of DAT. Moreover, the mechanism by which the BNIR system enhances wound healing through the modulation of endogenous electric fields necessitates further investigation. Additional empirical

evidence is required, as it will significantly contribute to the clinical translation and application of the BNIR system.

3. Conclusions

Inspired by the electrophysiological environment and structure of skin tissue, we developed a bionic neuro-immuno-regulatory (BNIR) system to promote diabetic wound healing. The BNIR system comprises microporous structure scaffolds and nanosheets and enables swift biofluid collection and electrical signal transmission. A freeze-forming technique was employed to construct a 3D DAT sponge scaffold for managing wound exudate and hemostasis. pMXene@bFGF exhibited enhanced ambient stability and antioxidative properties while maintaining conductivity. *In vitro*, DAT-pMXene@bFGF demonstrated excellent biocompatibility, enhancing cell proliferation, angiogenesis, and migration. Importantly, it facilitated the transition of M1 to M2 macrophages through neuro-immuno-regulatory. In a diabetic rat model, the BNIR system accelerated wound healing by promoting wound closure through aggregating wound exudate, coupling endogenous EF, neuro-immuno-regulatory, scavenging ROS, and delivering bFGF. The BNIR system also shows potential for regenerating other electrosensitive tissues such as cardiac and bone tissue.

4. Experimental section

4.1. Preparation and characterization of pMXene nanosheets

Ti_3C_2 nanosheets were synthesized through the acid etching of Ti_3AlC_2 powders (MAX phases, <38 μm) using a previously established method [53]. Specifically, 1 g of Ti_3AlC_2 (Jilin 11 technology Co., Ltd) was introduced into a mixture containing 1 g of LiF (Sigma-Aldrich, USA) and 20 mL of HCl solution (37 wt%, Sinopharm, China) at 35 °C with constant stirring for 24 h to facilitate the extraction of Al. After that, the resulting suspension was thoroughly washed with deionized water until its pH exceeded 5. The suspension was then centrifuged to collect the multilayered Ti_3C_2 MXene sediment. This MXene sediment underwent an additional step of sonication for 1 h. After centrifugation, the collected dark-green supernatant containing delaminated Ti_3C_2 nanosheets was subjected to freeze-drying. Then, a dopamine hydrochloride solution (2 mg mL^{-1}) was carefully introduced dropwise into 10 mL of Ti_3C_2 aqueous dispersion (2 mg mL^{-1}) at specified mass ratios (Ti_3C_2: dopamine hydrochloride at 100:6). Subsequently, the dispersion underwent further stirring (200 rpm, 30 °C) for 1 h and was then subjected to centrifugation to eliminate any unreacted monomers in the solution. The resulting sediment was redispersed in deionized water using ultrasound, yielding the polydopamine-modified MXene (pMXene) dispersion. Atomic Force Microscopy (AFM, Bruker Dimension Icon, Germany) was employed for the characterization of both the morphology and thickness of MXene nanosheets. Furthermore, Transmission Electron Microscopy (TEM, JEOL JEM 2100F, voltage of 300 kV), XPS measurements using an X-ray photoelectron spectrometer (Thermo Scientific, USA, working voltage of 12 kV), X-ray diffraction analysis (XRD, Rigaku Ultima IV, Japan) at a scanning speed of 10°/min over a range of 5°–80°, were performed to characterize MXene, pMXene nanosheets. Raman spectra were obtained using a high-resolution confocal Raman microscope (Renishaw inVia, UK) at room temperature.
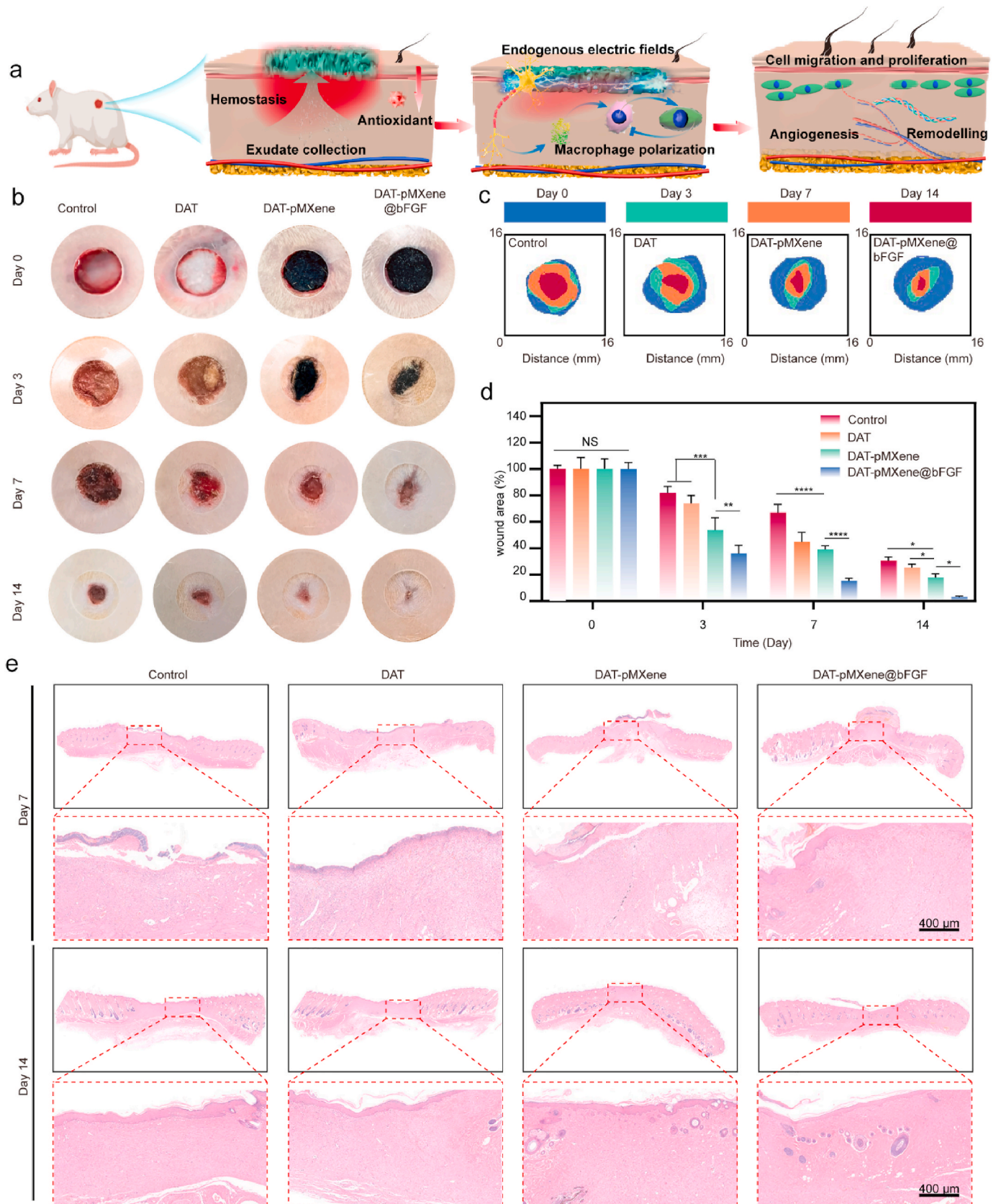
Fig. 6. Effects of composite scaffolds on facilitating the healing of diabetic wounds *in vivo*. (a) Schematic illustration illustrating the enhanced wound closure promoted by DAT-pMXene@bFGF scaffolds. (b) Representative photographs showcasing wounds in the diverse treatment groups. The inner diameter of the transparent reference was recorded as 10 mm. (c) The wound trace was observed in different groups on days 0, 3, 7, and 14. (d) Quantification of the wound area in different groups on days 0, 3, 7, and 14 (n = 3). (e) Representative H&E staining images of wounds on days 7 and 14.
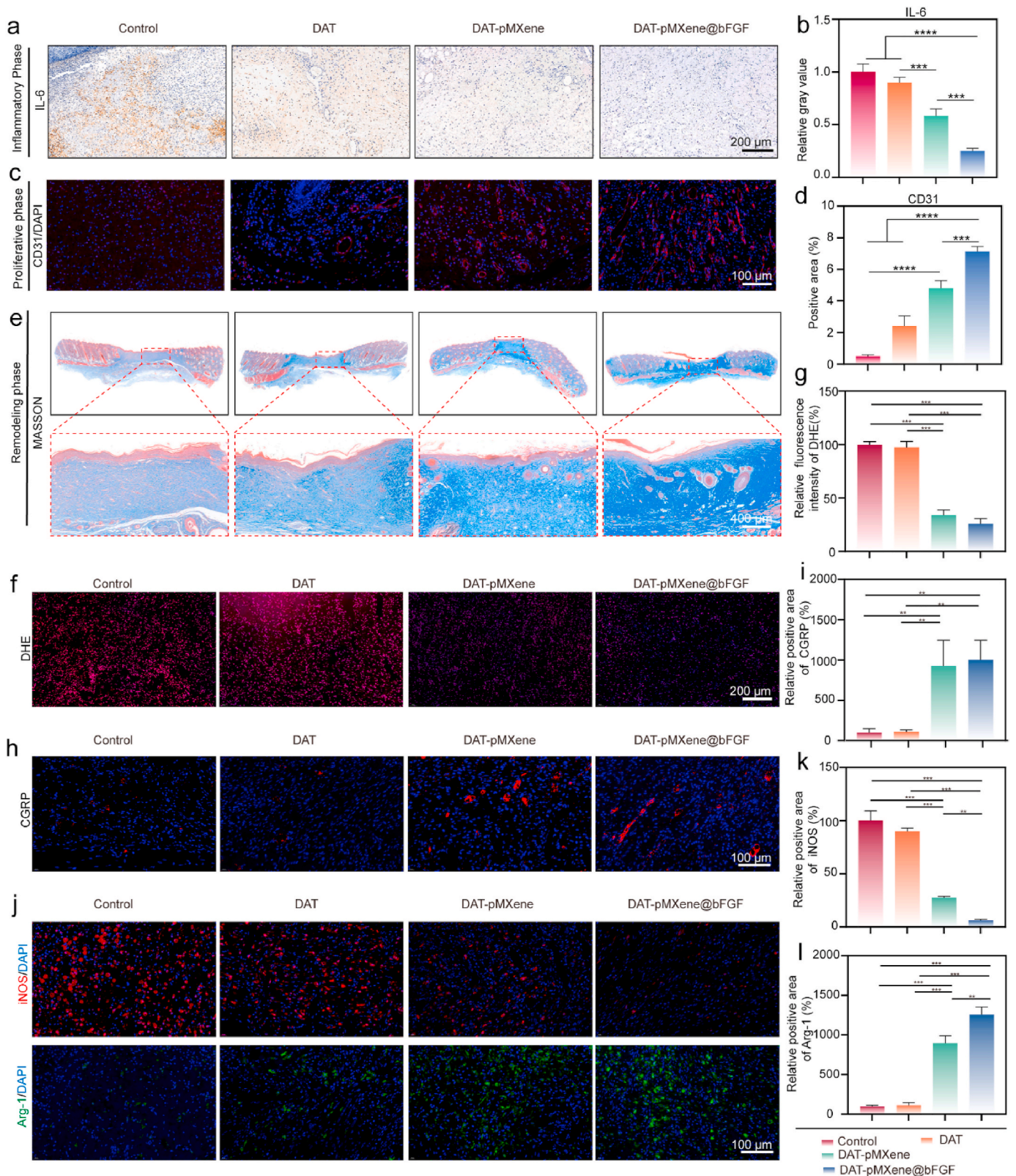
Fig. 7. *In vivo* studies for composite scaffolds-mediated acceleration of the three phases in diabetic wound repair, and the effect of composite scaffolds on anti-oxidation, neuromodulatory, and macrophage polarization. (a) Representative Immunohistochemical images of IL-6 on day 7. (b) Quantification of IL-6 (n = 3). (c) Representative immunofluorescent images displaying CD31 (red) on day 7. (d) Quantification of CD31 (n = 3). (e) Representative images of Masson's trichrome staining on day 14. (f, g) Detection of ROS levels in the wound bed using the DHE probe. (h) Representative immunofluorescent images of calcitonin gene-related peptide on day 7. (i) Quantification of calcitonin gene-related peptide (n = 3). (j) Representative immunofluorescent images depicting iNOS (red), and Arg-1 (green) expression *in vivo*. Quantification of (k) iNOS, and (l) Arg-1 (n = 3). Significance levels were denoted as *$P < 0.05$, **$P < 0.01$, ***$P < 0.001$, and ****$P < 0.0001$, to indicate statistical significance.

4.2. Preparation and characterization of pMXene@bFGF nanosheets

The collected pMXene nanosheets (10 mg) were immersed in a 10 mL solution of recombinant human basic fibroblast growth factor (bFGF, Nanhai Longtime Pharmaceutical Co., Ltd Guangdong, China) with a concentration of 1.0 mg mL^{-1} and stirred continuously for 12 h bFGF binding was investigated through UV–Vis spectroscopy (Thermo Scientific, USA). To assess bFGF loading efficiency, we utilized a BCA protein kit (Beyotime Biotechnology, China) to measure the residual concentration of bFGF in the total supernatant and determined the amount of remaining bFGF. The efficiency of bFGF loading was subsequently computed using the formula: (mass of bFGF - mass of residual bFGF)/ (mass of bFGF). UV–Vis spectroscopy (Thermo Scientific, USA), Dynamic Light Scattering (DLS), and Zeta potential (Malvern Zetasizer Nano ZS90, UK) were performed to characterize MXene, pMXene and pMXene@bFGF nanosheets.

4.3. bFGF release

pMXene@bFGF nanosheets were subjected to incubation in 2 mL PBS with agitation at 200 rpm and a temperature of 37 °C. At predetermined intervals, 500 μL of the released medium was withdrawn and centrifuged at 10000 rpm. At every time interval, 500 μL of the storage solution was obtained for measurement, and a corresponding volume of fresh PBS (500 μL) was added. The bFGF released from p-MXene@bFGF nanosheets was determined using a BCA protein assay kit (Beyotime Biotechnology, China). According to the instructions, the BCA working solution was prepared and added to the samples. The absorbance of the mixed solution at 562 nm was measured using a microplate reader (Thermo Fisher, USA). The concentration of the released bFGF was then calculated based on the standard curve.

4.4. Preparation of DAT-pMXene@bFGF scaffolds

Adipose tissue harvested from porcine subcutaneous fat was decellularized following the protocol previously established by our research team, aiming to isolate the extracellular matrix of adipose tissue [54]. The obtained DAT was cut into fragments and homogenized to form a suspension with a concentration of 20 mg mL^{-1} using a homogenizer. The DAT suspension is introduced into a mold and subjected to the process of freeze-drying. A 100 mg DAT scaffold was immersed in a 10 mL suspension of 1 mg mL^{-1} pMXene@bFGF and left to incubate overnight on a shaker at 37 °C. Then, the composite scaffold is extracted and subjected to triple rinsing with deionized water, followed by freeze-drying for subsequent utilization.

4.5. Characterization of DAT, DAT-pMXene, and DAT-pMXene@bFGF scaffolds

The native and decellularized tissues were immersed in 4 % paraformaldehyde for fixation, subsequently embedded in paraffin and sectioned. The obtained sections underwent deparaffinization and ethanol-based dehydration. Hematoxylin and eosin (H&E, servicebio, China) staining, Masson's trichrome staining (servicebio, China), oil red O staining (servicebio, China), and immunofluorescent staining with DAPI (Beyotime Biotechnology, China) were employed for identifying any remaining cells or cellular fragments and assessing the collagen structure within the DAT. DAT, DAT-pMXene, and DAT-pMXene@bFGF scaffolds were additionally characterized using X-ray diffraction analysis (XRD, Rigaku Ultima IV, Japan) at a scanning speed of 10°/min over a range of 5°–80°, FTIR (Thermo Scientific Nicolet iS5, USA, recording range: 400–4000 cm^{-1}, at a resolution 4 cm^{-1}), scanning electron microscopy (SEM) images and EDS mapping (ZEISS Sigma 300, Germany). In addition, bFGF was characterized by FTIR (Thermo Scientific Nicolet iS5, USA). The thermogravimetric analysis (TGA) of DAT, DAT-pMXene and DAT-pMXene@bFGF was conducted using a thermogravimetric

analyzer (TA Q500, USA). The temperature range assessed in this study encompassed 30–800 °C. The furnace was operated at a heating rate of 20 °C min^{-1}.

4.6. Swelling ratio, mechanical properties, conductivity, and degradation of the composite scaffolds

The composite scaffolds were initially weighed (W$_I$) after equilibrating in PBS at 37 °C and subjected to shaking incubation at 100 rpm. At specified time intervals, the composite scaffolds were extracted, and the surface water was removed using filter paper. After undergoing lyophilization, they were reweighed (W$_O$). The swelling ratio (SR) was determined using the formula:

$$SR = (W_I - W_O) /\ W_O \times 100\%$$

The mechanical properties of the composite scaffolds were assessed using a mechanical testing instrument (HY-940FS, China), with stress-strain curves recorded. Compressive tests were performed at 5 mm/min up to 80 % strain, with Young's modulus calculated from the slope of the stress-strain curve between 10 % and 15 % strain.

The conductivity of the composite scaffolds was assessed following established literature [18].

Briefly, the conductivity of the composite scaffolds was measured with a four-probe resistivity system (Jingge, Suzhou, China). The composite scaffolds were pressed into tablets (10 mm diameter, 0.5 mm height) for testing.

The scaffolds of identical mass were incubated in vials containing PBS and collagenase I (2 U/ml) at 37 °C for specific time intervals. Following lyophilization, the samples were retrieved and weighed. The residual weight ratio of the samples was determined using the formula below:

$$\text{Weight remaining ratio (\%)} = W_t/W_0 \times 100\%$$

Where W$_0$ represents the initial weight of the scaffolds, and W$_t$ denotes the weight of the residual scaffolds after specified degradation intervals. In addition, the electrical and antioxidant properties of the scaffolds after degradation were also evaluated.

4.7. Porosity test

The porosity of the scaffolds was evaluated using the liquid displacement method [55]. Ethanol (Aladdin, Shanghai, China) was chosen as the replacement liquid. A volume of ethanol (V$_0$) was added to a graduated cylinder, and the sample was immersed until saturated, recording the scale (V$_1$). The sample was removed, and the remaining solution volume (V$_2$) was recorded. The porosity was calculated using the formula: Porosity (%) = (V$_0$ - V$_2$)/(V$_1$-V$_2$) × 100 %

4.8. Evaluations of red blood cell adhesion and liver hemostatic

The composite scaffolds were exposed to whole blood for 5 min at 37 °C. Then, all samples underwent three washes with PBS to eliminate free blood cells. The samples were fixed in 2.5 % glutaraldehyde for 2 h, then dehydrated in a series of ethanol concentrations, and observed using SEM (ZEISS Sigma 300, Germany). Moreover, *in vivo*, coagulation tests were performed on rat liver. A skin perforator with a 5 mm diameter was used to create a 3 mm deep hole at the liver lobe. Once the perforator was removed, Gauze, DAT, and DAT-pMXene@bFGF scaffolds were applied to the wound surface. In the control group, no treatment was administered.

4.9. Cell culture

NIH-3T3 cells, human umbilical vein endothelial cells (HUVECs), and Raw 264.7 cells were obtained from the Cell Bank of the Chinese Academy of Sciences (Shanghai, China). Schwann cells (SCs) were

purchased from ATCC. All cells were cultured in high-glucose DMEM (Gibco, USA) with 10 % FBS (Gibco, USA) and 1 % penicillin-streptomycin (Invitrogen, USA) under 5 % CO₂.

4.10. Biocompatibility evaluation

NIH-3T3 cells and human umbilical vein endothelial cells (HUVECs) were selected to evaluate the biocompatibility of the composite scaffolds. The cell viability of NIH-3T3 and HUVECs on the scaffolds was assessed *via* live-dead staining (calcein AM/PI staining kit Beyotime Biotechnology, China) following a one-day culture period. To examine cell morphology, a staining protocol was implemented, utilizing phalloidin (Beyotime Biotechnology, China) for 30min and DAPI (Beyotime Biotechnology, China) for 5 min at room temperature. Imaging was then conducted using a fluorescence microscope. Furthermore, NIH-3T3 and HUVECs were cultured with the different scaffolds, each well seeded with 8.0×10^3 cells, and maintained at 37 °C in a humidified incubator with 5 % CO₂. Cytotoxicity was determined at 1, 3, and 5 days postculture using the CCK-8 assay (CCK-8 kit, Beyotime Biotechnology, China) and live-dead staining (calcein AM/PI staining kit, Beyotime Biotechnology, China), following the guidelines provided by the manufacturer. In addition, following sterilization of the scaffolds, they were transferred to 24-well plates. The scaffolds were pretreated by PBS for 15 min. Subsequently, HUVECs and NIH-3T3 cells were separately seeded onto the scaffolds surface and cultured for 24 h. Cells adherent to the scaffolds were fixed in 2.5 % glutaraldehyde (Aladdin, Shanghai, China), dehydrated using graded ethanol (Aladdin, Shanghai, China), and subsequently analyzed by SEM. Moreover, the blood compatibility of the composite scaffolds was assessed through a hemolysis activity assay. In brief, 500 μL of rat blood was collected, and 5 ml of PBS was added, followed by centrifugation at 2000 rpm for 5 min. The lower erythrocytes were washed with PBS through three additional centrifugation steps and resuspended in 10 mL of PBS. Then, 5 mg of the composite scaffold sample in each group was introduced to 1 mL of red blood cells in a tube, and the mixture was incubated at room temperature for 4 h. To determine the degree of hemolysis, the experiment included a negative control (PBS) and a positive control (water). The measurement of hemoglobin absorbance in the supernatant was performed using a microplate reader at 577 nm. The hemolysis ratio for each group was determined using the following formula:

$$\text{Hemolysis} = (As - An) / (Ap - An) \times 100\%$$

Here, As, Ap, and An denote the absorbance values of the sample, positive control, and negative control groups, respectively.

4.11. Tube formation assay

To assess the angiogenic potential of the composite scaffolds, growth factor-reduced Matrigel (50 μL per well, Corning, USA) was used. In brief, matrigel was evenly distributed in a pre-cooled 96-well plate and allowed to solidify at 37 °C for 1 h. Subsequently, 100 μL of HUVEC suspension in pure DMEM, DMEM with the extracts of the composite scaffolds was seeded onto the Matrigel-coated 96-well plate at a density of 4×10^4 cells mL^{-1}. Following incubation at 37 °C for 4 h, cellular observations were conducted using a microscope (Leica, Germany).

4.12. Cell migration

The evaluation of cell migration was performed using the transwell cell migration assay. HUVECs and NIH-3T3 cells were selected to evaluate the composite scaffold's ability to promote cell migration. In brief, the composite scaffolds were positioned in the lower chamber of a transwell insert, with approximately 2×10^4 HUVECs or NIH-3T3 cells per well in the upper chamber, and subsequent incubation lasted for 24 h. After eliminating non-migrated cells with a dry cotton swab, the transmigrated cells were fixed and subsequently stained with crystal violet. Subsequently, the cells that had transmigrated were examined using a microscope. Furthermore, the scratch test was further employed to assess the migration of HUVECs. HUVECs were cultivated in 6-well plates treated with the composite scaffolds, allowing them to reach a confluence of at least 90 % before conducting the scratch tests. Subsequently, a scratch wound was generated using a 10 μL pipette tip. After 24 h, the scaffold was removed, followed by PBS washing, and observation and photography were conducted using a microscope.

In addition, the transwell cell migration assay was performed to investigate the impact of Schwann cells (SCs) and DAT-pMXene@bFGF scaffolds on macrophage migration utilizing the aforementioned methods. Briefly, 5×10^4 SCs per well and DAT-pMXene@bFGF scaffolds were first placed in the lower wells of 24-well culture plates, followed by the introduction of2×10^4 Raw 264.7 cells per well into the upper chambers of transwell inserts, and subsequent incubation lasted for 24 h. After eliminating non-migrated cells with a dry cotton swab, the transmigrated cells were fixed and subsequently stained with crystal violet.

4.13. Free radical scavenging assay

The antioxidant capability of the scaffolds was examined using DPPH (Aladdin, Shanghai, China) and ABTS (Aladdin, Shanghai, China) free radical scavenging assay and ROS assay.

In the DPPH assay, a DPPH solution in ethanol, pre-prepared at a concentration of 0.04 mg mL^{-1}, was employed. Subsequently, the composite scaffolds were mixed with 3 mL of the DPPH solution and left to react for 20 min. Finally, UV–vis spectroscopy was employed to measure the absorbance at 517 nm. In addition, the UV absorbance of the solution was measured at various time points to evaluate its DPPH scavenging activity.

In the ABTS assay, 0.4 mL of ABTS solution (7.4 mmol L^{-1}) with an equal volume of a 2.6 mmol L^{-1} potassium persulfate solution was employed to generate ABTS●+. Following that, the solution underwent a 50-fold dilution with PBS buffer for subsequent reaction with the composite scaffolds. After the ABTS and scaffold reaction, a 20 min incubation preceded the measurement of absorbance at 734 nm using UV–vis spectroscopy. In addition, the UV absorbance of the solution was measured at various time points to evaluate its ABTS scavenging activity.

The inhibition rate of DPPH and ABTS was calculated as follows:

$$\text{Inhibition}(\%) = (A_I - A) / A_I \times 100\%$$

Where A_I represents the absorbance without the scaffolds, and A denotes the absorbance with the scaffolds.

To evaluate the scaffold's ability to scavenge ROS. ESR spectroscopy was used to detect the elimination of hydroxyl radical (●OH), superoxide anion (●O₂−), and hydrogen peroxide (H_2O_2).

4.14. ROS scavenging activity and mitochondrial membrane potential detection

H_2O_2 was chosen to induce exogenous oxidative stresses on HUVECs, and NIH-3T3 cells to assess the antioxidant capability of the composite scaffolds. HUVECs and NIH-3T3 were incubated with H_2O_2 (100 μM), and the composite scaffolds in 24-well plates for 24 h using DMEM. ROS levels were measured with the ROS assay kit according to the manufacturer's instructions. For the measurement of the mitochondrial membrane potentials of HUVECs and NIH-3T3, cells were stained with the Mitochondrial Membrane Potential Assay Kit for 20 min and subsequently observed using the microscope.

4.15. Effects of DAT-pMXene@bFGF scaffolds on schwann cell

SCs and DAT-pMXene@bFGF scaffolds were co-cultured. Cell viability was evaluated *via* live/dead staining. In addition, the cells were

treated with 4 % paraformaldehyde for fixation, permeabilized with Triton X-100, and blocked using 5 % bovine serum albumin. Then, the cells were labeled with goat anti-rabbit S100-β (1:100, Abcam) and goat anti-rabbit GFAP (1:100, Abcam) overnight at 4 °C. Samples were treated with secondary antibodies, then stained with phalloidin at 37 °C for 30 min, and counterstained with DAPI at room temperature for 5 min.

4.16. In vitro evaluation of macrophage polarization

To evaluate the effects of the composite scaffolds and SCs on macrophage polarization, Raw 264.7 cells were initially cultured for 24 h and then exposed to a medium containing LPS (100 ng mL^{-1}, Aladdin, Shanghai, China) for an additional 24 h. Subsequently, the composite scaffolds, SCs, and Raw 264.7 cells were co-cultured for 48 h. Raw 264.7 cells were in the lower chamber, while DAT-pMXene@bFGF scaffolds and SCs were in the upper chamber. Immunofluorescent staining was employed to detect the expression of M1 and M2 surface markers (CD86 and CD206). In brief, RAW264.7 cells were fixed with a 4 % paraformaldehyde solution after treatment, permeabilized with 0.5 % Triton X-100, and blocked with 5 % BSA. Then, the cells were labeled with rabbit antimouse CD206 (1:50, Beyotime Biotechnology, China) and rabbit antimouse CD86 (1:50, Beyotime Biotechnology, China) overnight at 4 °C. The next day, Alexa Fluor 488-labeled goat anti-mouse antibody (1:500, Beyotime Biotechnology, China) or Cy3-labeled Goat Anti-Mouse antibody (1:500, Beyotime Biotechnology, China) was applied to interact with the primary antibody. Afterward, DAPI was used to counterstain the cell nuclei, and the samples were observed through microscopy. Additionally, flow cytometry was used to assess the ratio of M1 and M2 macrophages. Specifically, 1×10^6 cells were harvested and exposed to 100 μL of PBS containing CD86 and CD206 antibodies (BioLegend, San Diego, USA). Ultimately, the expressions of CD86 and CD206 on RAW264.7 cells were identified using a flow cytometer (FC BD LSR Fortessa X-20).

4.17. qPCR analysis

The gene expression of Arg-1, IL-10, iNOS, and IL-6 in RAW264.7 cells was examined. 1×10^6 macrophages were co-cultured with the composite scaffolds and SCs for 48 h in the presence of LPS (100 ng mL^{-1}) to mimic an inflammatory microenvironment. Subsequently, total RNA was isolated using an RNA Purification Kit (Vazyme Biotech, Nanjing) following the manufacturer's instructions. The primer sequences can be found in Table S1.

4.18. Western blotting

Following standard protein lysis, electrophoresis, and membrane transfer procedures, the membrane was incubated with a blocking buffer (Beyotime, China). Subsequently, the membranes were exposed to specific primary antibodies against GAPDH (1:1000, CST), NF-κB (1:1000, p65, CST), NF-κB (1:1000, p-p65 CST), NF-κB (1:1000, IκB, CST), NF-κB (1:1000, p-IκB CST) iNOS (1:1000, CST), TNF-α (1:1000, Abcam), IL-10 (1:1000, CST), overnight at 4 °C, followed by secondary antibodies at 37 °C.

4.19. Preparation of diabetic rat models and assessment of wound healing

All surgical procedures strictly adhered to the guidelines of the National Institutes of Health (NIH) for the care and use of laboratory animals. The study was approved by the Animal Ethics Committee of Shanghai Tenth People's Hospital affiliated with Tongji University School of Medicine (approval number: SHDSYY-2023-25301). Sprague-Dawley (SD) rats weighing 200–250 g were induced into diabetes by intraperitoneal injection of a pre-prepared streptozotocin (STZ, Macklin Biochemical Co., Ltd) solution at a dose of 70 mg kg^{-1}. After three

consecutive days of injections, rats that demonstrated blood glucose levels exceeding 16.7 mmol L^{-1} were acknowledged as successfully model established and then randomly allocated into four groups: Control, DAT, DAT-pMXene, and DAT-pMXene@bFGF. Subsequently, circular full-thickness excisional wounds (diameter: 10 mm) were created on the dorsal area of each rat. Wound healing progress was documented with a digital camera at intervals of 3, 7, and 14 days following treatment. The data was processed using the Image J software for analysis. The wound healing percentage was evaluated using the formula:

$$\text{Wound healing percentage} = (A_i - A_t) / A_i \times 100 \%$$

Where A_i stands for the initial wound area, while A_t represents the remaining wound area at each time point.

4.20. Histological analysis and immunohistochemical staining

At a specified time point, all the rats were sacrificed, and the collected specimens were fixed in 4 % paraformaldehyde. Following fixation, the specimens were embedded in paraffin for subsequent evaluations. Hematoxylin and eosin (H&E, servicebio, China) staining were conducted to assess the extent of wound closure. Furthermore, vital organs (heart, lung, liver, spleen, and kidney) were processed for histological analysis. Masson's trichrome staining was employed for the quantification of collagen deposition. For evaluating the degree of inflammation, the immunostaining for IL-6 (servicebio, China), and TNF-α (servicebio, China) was carried out following the prescribed protocols provided by the manufacturer. Furthermore, immunohistochemical staining for CD31 (servicebio, China), and α-SMA (servicebio, China) was conducted to demonstrate the presence of newly formed blood vessels. For the analysis of *in vivo* superoxide levels, the level of ROS on the 7th day was determined using DHE staining (servicebio, China). Furthermore, immunofluorescence staining was performed for CGPR (servicebio, China), Arg-1 (servicebio, China), and iNOS (servicebio, China) to assess neuro-immuno-regulatory. The images were acquired using a digital microscope (Leica, USA).

4.21. Statistical analysis

All biological experiments were conducted in triplicate unless otherwise stated. The data was represented as mean ± standard deviation and statistical analysis was performed using GraphPad Prism software. A one-way analysis of variance (ANOVA) was used to perform statistical analysis for multiple comparisons, followed by Tukey's post hoc test. Significance levels were denoted as $*P < 0.05$, $**P < 0.01$, $***P < 0.001$, and $****P < 0.0001$, to indicate statistical significance. ns = not significant.

CRediT authorship contribution statement

Zhiqing Liu: Writing – review & editing, Writing – original draft, Visualization, Methodology, Investigation, Formal analysis, Conceptualization. **Tianlong Wang:** Methodology, Investigation. **Jinhui Zhao:** Methodology, Conceptualization. **Lei Zhang:** Investigation, Conceptualization. **Yiping Luo:** Validation, Methodology, Investigation. **Yixing Chen:** Methodology, Investigation. **Xinhui Wu:** Formal analysis, Data curation. **Yaqi Liu:** Methodology, Investigation. **Aihemaitijiang Aierken:** Methodology. **Dilixiati Duolikun:** Investigation, Formal analysis. **Hui Jiang:** Conceptualization. **Xinyu Zhao:** Conceptualization. **Chang Li:** Writing – review & editing. **Yingchuan Li:** Conceptualization. **Wentao Cao:** Writing – review & editing, Writing – original draft, Investigation, Funding acquisition. **Jianzhong Du:** Writing – review & editing, Funding acquisition, Conceptualization. **Longpo Zheng:** Funding acquisition, Conceptualization.

Data availability statement

The data that support the findings of this study are available from the corresponding author upon reasonable request.

Ethics approval and consent to participate

All surgical procedures strictly adhered to the guidelines of the National Institutes of Health (NIH) for the care and use of laboratory animals. The study was approved by the Animal Ethics Committee of Shanghai Tenth People's Hospital affiliated with Tongji University School of Medicine (approval number: SHDSYY-2023-25301).

Declaration of competing interest

The authors declare no conflict of interest.

Acknowledgments

Appendix A. Supplementary data

Supplementary data to this article can be found online at https://doi.org/10.1016/j.bioactmat.2025.01.024.

References

[1] W. Li, S. Wu, L. Ren, B. Feng, Z. Chen, Z. Li, B. Cheng, J. Xia, Development of an antiswelling hydrogel system incorporating M2-exosomes and photothermal effect for diabetic wound healing, ACS Nano 17 (21) (2023) 22106–22120.

[2] Y. Xiong, Z. Lin, P. Bu, T. Yu, Y. Endo, W. Zhou, Y. Sun, F. Cao, G. Dai, Y. Hu, L. Lu, L. Chen, P. Cheng, K. Zha, M.A. Shahbazi, Q. Feng, B. Mi, G. Liu, A whole-course-repair system based on neurogenesis-angiogenesis crosstalk and macrophage reprogramming promotes diabetic wound healing, Adv. Mater. 35 (19) (2023) e2212300.

[3] L. Bai, M. Feng, Q. Zhang, Z. Cai, Q. Li, Y. Li, C. Ma, J. Xiao, Y. Lin, Synergistic osteogenic and antiapoptotic framework nucleic acid complexes prevent diabetic osteoporosis, Adv. Funct. Mater. 34 (28) (2024).

[4] Y. Li, R. Fu, Z. Duan, C. Zhu, D. Fan, Artificial nonenzymatic antioxidant MXene nanosheet-anchored injectable hydrogel as a mild photothermal-controlled oxygen release platform for diabetic wound healing, ACS Nano 16 (5) (2022) 7486–7502.

[5] L. Yang, D. Zhang, W. Li, H. Lin, C. Ding, Q. Liu, L. Wang, Z. Li, L. Mei, H. Chen, Y. Zhao, X. Zeng, Biofilm microenvironment triggered self-enhancing photodynamic immunomodulatory microneedle for diabetic wound therapy, Nat. Commun. 14 (1) (2023) 7658.

[6] Z. Tu, M. Chen, M. Wang, Z. Shao, X. Jiang, K. Wang, Z. Yao, S. Yang, X. Zhang, W. Gao, C. Lin, B. Lei, C. Mao, Engineering bioactive M2 macrophage-polarized anti-inflammatory, antioxidant, and antibacterial scaffolds for rapid angiogenesis and diabetic wound repair, Adv. Funct. Mater. 31 (30) (2021).

[7] Y.J. Fu, Y.F. Shi, L.Y. Wang, Y.F. Zhao, R.K. Wang, K. Li, S.T. Zhang, X.J. Zha, W. Wang, X. Zhao, W. Yang, All-natural immunomodulatory bioadhesive hydrogel promotes angiogenesis and diabetic wound healing by regulating macrophage heterogeneity, Adv Sci (Weinh) 10 (13) (2023) e2206771.

[8] T. Deng, D. Gao, X. Song, Z. Zhou, L. Zhou, M. Tao, Z. Jiang, L. Yang, L. Luo, A. Zhou, L. Hu, H. Qin, M. Wu, A natural biological adhesive from snail mucus for wound repair, Nat. Commun. 14 (1) (2023).

[9] W. Qin, L. Li, W. Niu, W.R. Wang, D.W. Wu, C.G. Song, C.H. Gao, Z. Mu, F.R. Tay, K. Jiao, L.N. Niu, Effects of electric field-modulated conductive hydrogel on osseoperception and osseointegration of dental implants, Adv. Funct. Mater. 34 (28) (2024).

[10] Y.W. Hu, Y.H. Wang, F. Yang, D.X. Liu, G.H. Lu, S.T. Li, Z.X. Wei, X. Shen, Z. D. Jiang, Y.F. Zhao, Q. Pang, B.Y. Song, Z.W. Shi, S. Shafique, K. Zhou, X.L. Chen,

[11] W.M. Su, J.W. Jian, K.Q. Tang, T.L. Liu, Y.B. Zhu, Flexible organic photovoltaic-powered hydrogel bioelectronic dressing with biomimetic electrical stimulation for healing infected diabetic wounds, Adv Sci (Weinh) 11 (10) (2024) e2307746.

[11] K. Wang, U. Parekh, J.K. Ting, N.A.D. Yamamoto, J. Zhu, T. Costantini, A.C. Arias, B.P. Eliceiri, T.N. Ng, A platform to study the effects of electrical stimulation on immune cell activation during wound healing, Adv. Biosyst. 3 (10) (2019).

[12] R. Luo, Y. Liang, J. Yang, H. Feng, Y. Chen, X. Jiang, Z. Zhang, J. Liu, Y. Bai, J. Xue, S. Chao, Y. Xi, X. Liu, E. Wang, D. Luo, Z. Li, J. Zhang, Reshaping the endogenous electric field to boost wound repair via electrogenerative dressing, Adv. Mater. 35 (16) (2023).

[13] C.D. McCaig, A.M. Rajnicek, B. Song, M. Zhao, Controlling cell behavior electrically: current views and future potential, Physiol. Rev. 85 (3) (2005) 943–978.

[14] X. Liu, Z. Cai, M. Pei, H. Zeng, L. Yang, W. Cao, X. Zhou, F. Chen, Bacterial cellulose-based bandages with integrated antibacteria and electrical stimulation for advanced wound management, Adv. Healthcare Mater. (2023) e2302893.

[15] W. Cao, S. Peng, Y. Yao, J. Xie, S. Li, C. Tu, C. Gao, A nanofibrous membrane loaded with doxycycline and printed with conductive hydrogel strips promotes diabetic wound healing in vivo, Acta Biomater. 152 (2022) 60–73.

[16] Y.Z. Lu, B. Nayer, S.K. Singh, Y.K. Alshoubaki, E. Yuan, A.J. Park, K. Maruyama, S. Akira, M.M. Martino, CGRP sensory neurons promote tissue healing via neutrophils and macrophages, Nature 628 (8008) (2024) 604–611.

[17] M. Zhao, Electrical fields in wound healing-An overriding signal that directs cell migration, Semin. Cell Dev. Biol. 20 (6) (2009) 674–682.

[18] J. Wang, J. Lin, L. Chen, L. Deng, W. Cui, Endogenous electric-field-coupled electrospun short fiber via collecting wound exudation, Adv. Mater. 34 (9) (2022).

[19] Z. Ge, W. Guo, Y. Tao, H. Sun, X. Meng, L. Cao, S. Zhang, W. Liu, M.L. Akhtar, Y. Li, Y. Ren, Wireless and closed-loop smart dressing for exudate management and on-demand treatment of chronic wounds, Adv. Mater. 35 (47) (2023) e2304005.

[20] S. Qian, J. Wang, Z. Liu, J. Mao, B. Zhao, X. Mao, L. Zhang, L. Cheng, Y. Zhang, X. Sun, W. Cui, Secretory fluid-aggregated janus electrospun short fiber scaffold for wound healing, Small 18 (36) (2022) e2200799.

[21] L.E. Flynn, The use of decellularized adipose tissue to provide an inductive microenvironment for the adipogenic differentiation of human adipose-derived stem cells, Biomaterials 31 (17) (2010) 4715–4724.

[22] T.T. Han, S. Toutounji, B.G. Amsden, L.E. Flynn, Adipose-derived stromal cells mediate in vivo adipogenesis, angiogenesis and inflammation in decellularized adipose tissue bioscaffolds, Biomaterials 72 (2015) 125–137.

[23] P. Luo, H. Huang, Y. Wu, X. Liu, Z. Shan, L. Gong, S. Deng, H. Liu, J. Fang, S. Wu, X. Wu, Q. Liu, Z. Chen, K.W.K. Yeung, W. Qiao, S. Chen, Z. Chen, Tailoring the multiscale mechanics of tunable decellularized extracellular matrix (dECM) for wound healing through immunomodulation, Bioact. Mater. 28 (2023) 95–111.

[24] J. Wang, Y. Cheng, H. Wang, Y. Wang, K. Zhang, C. Fan, H. Wang, X. Mo, Biomimetic and hierarchical nerve conduits from multifunctional nanofibers for guided peripheral nerve regeneration, Acta Biomater. 117 (2020) 180–191.

[25] S. Li, T. Tian, T. Zhang, Y. Lin, X. Cai, A bioswitchable delivery system for microRNA therapeutics based on a tetrahedral DNA nanostructure, Nat. Protoc. (2024).

[26] L. Mao, S. Hu, Y. Gao, L. Wang, W. Zhao, L. Fu, H. Cheng, L. Xia, S. Xie, W. Ye, Z. Shi, G. Yang, Biodegradable and electroactive regenerated bacterial cellulose/MXene (Ti3C2Tx) composite hydrogel as wound dressing for accelerating skin wound healing under electrical stimulation, Adv. Healthcare Mater. 9 (19) (2020).

[27] C. Geng, S. He, S. Yu, H.M. Johnson, H. Shi, Y. Chen, Y.K. Chan, W. He, M. Qin, X. Li, Y. Deng, Achieving clearance of drug-resistant bacterial infection and rapid cutaneous wound regeneration using an ROS-balancing-engineered heterojunction, Adv. Mater. 36 (16) (2024) e2310599.

[28] W.T. Cao, C. Ma, D.S. Mao, J. Zhang, M.G. Ma, F. Chen, MXene-reinforced cellulose nanofibril inks for 3D-printed smart fibres and textiles, Adv. Funct. Mater. 29 (51) (2019).

[29] I.K. Han, K.I. Song, S.M. Jung, Y. Jo, J. Kwon, T. Chung, S. Yoo, J. Jang, Y.T. Kim, D.S. Hwang, Y.S. Kim, Electroconductive, adhesive, non-swelling, and viscoelastic hydrogels for bioelectronics, Adv. Mater. 35 (4) (2023) e2203431.

[30] F.F.F. Garrudo, L.F.V. Ferreira, A.M. Ferraria, A.M.B. do Rego, A. Charas, V. André, M.T. Duarte, R.J. Linhardt, F.C. Ferreira, J. Morgado, Pseudo-doping effect on structural and electrical properties of polyaniline-camphorsulfonic acid, Synth. Met. 301 (2024).

[31] X. Luo, L. Zhang, Y. Luo, Z. Cai, H. Zeng, T. Wang, Z. Liu, Y. Chen, X. Sheng, A.E.d. G. Mandlate, Z. Zhou, F. Chen, L. Zheng, Charge-driven self-assembled microspheres hydrogel scaffolds for combined drug delivery and photothermal therapy of diabetic wounds, Adv. Funct. Mater. 33 (26) (2023).

[32] Y. Li, H. Luo, Y. Li, P. Huang, J. Xu, J. Zhang, P. Cai, H. He, J. Wu, X. Li, Surface biofunctional bFGF-loaded electrospun suture accelerates incisional wound healing, Mater. Des. 225 (2023).

[33] X. Han, J. Huang, H. Lin, Z. Wang, P. Li, Y. Chen, 2D ultrathin MXene-based drug-delivery nanoplatform for synergistic photothermal ablation and chemotherapy of cancer, Adv. Healthcare Mater. 7 (9) (2018) e1701394.

[34] S. Xu, C. Du, M. Zhang, R. Wang, W. Feng, C. Wang, Q. Liu, W. Zhao, Electroactive and antibacterial wound dressings based on Ti3C2Tx MXene/poly(ε-caprolactone)/gelatin coaxial electrospun nanofibrous membranes, Nano Res. 16 (7) (2023) 9672–9687.

[35] N. Nguyen, Z.-H. Lin, S.R. Barman, C. Korupalli, J.-Y. Cheng, N.-X. Song, Y. Chang, F.-L. Mi, H.-L. Song, H.-W. Sung, Y.-J. Lin, Engineering an integrated electroactive dressing to accelerate wound healing and monitor noninvasively progress of healing, Nano Energy 99 (2022).

[36] L. Qiao, Y. Liang, J. Chen, Y. Huang, S.A. Alsareii, A.M. Alamri, F.A. Harraz, B. Guo, Antibacterial conductive self-healing hydrogel wound dressing with dual

dynamic bonds promotes infected wound healing, Bioact. Mater. 30 (2023) 129–141.

[37] C.Y. Zou, X.X. Lei, J.J. Hu, Y.L. Jiang, Q.J. Li, Y.T. Song, Q.Y. Zhang, J. Li-Ling, H. Q. Xie, Multi-crosslinking hydrogels with robust bio-adhesion and pro-coagulant activity for first-aid hemostasis and infected wound healing, Bioact. Mater. 16 (2022) 388–402.

[38] X. Han, S. Chen, Z. Cai, Y. Zhu, W. Yi, M. Guan, B. Liao, Y. Zhang, J. Shen, W. Cui, D. Bai, A diagnostic and therapeutic hydrogel to promote vascularization via blood sugar reduction for wound healing, Adv. Funct. Mater. 33 (14) (2023).

[39] Z. Li, Y. Zhao, H. Huang, C. Zhang, H. Liu, Z. Wang, M. Yi, N. Xie, Y. Shen, X. Ren, J. Wang, J. Wang, A nanozyme-immobilized hydrogel with endogenous ROS-scavenging and oxygen generation abilities for significantly promoting oxidative diabetic wound healing, Adv. Healthcare Mater. 11 (22) (2022) e2201524.

[40] W. Feng, X. Han, H. Hu, M. Chang, L. Ding, H. Xiang, Y. Chen, Y. Li, 2D vanadium carbide MXenzyme to alleviate ROS-mediated inflammatory and neurodegenerative diseases, Nat. Commun. 12 (1) (2021) 2203.

[41] H. Lu, J. Wei, K. Liu, Z. Li, T. Xu, D. Yang, Q. Gao, H. Xiang, G. Li, Y. Chen, Radical-scavenging and subchondral bone-regenerating nanomedicine for osteoarthritis treatment, ACS Nano 17 (6) (2023) 6131–6146.

[42] J. Hou, H. Wang, Z. Ge, T. Zuo, Q. Chen, X. Liu, S. Mou, C. Fan, Y. Xie, L. Wang, Treating acute kidney injury with antioxidative black phosphorus nanosheets, Nano Lett. 20 (2) (2020) 1447–1454.

[43] J. Chen, Y. Liu, G. Cheng, J. Guo, S. Du, J. Qiu, C. Wang, C. Li, X. Yang, T. Chen, Z. Chen, Tailored hydrogel delivering niobium carbide boosts ROS-scavenging and antimicrobial activities for diabetic wound healing, Small 18 (27) (2022).

[44] Z. Liu, X. Wan, Z.L. Wang, L. Li, Electroactive biomaterials and systems for cell fate determination and tissue regeneration: design and applications, Adv. Mater. 33 (32) (2021).

[45] S.J. Zhang, W.L. Wu, K.Y. Yang, Y.Z. Chen, H.C. Liu, Phenotypic changes of Schwann cells on the proximal stump of injured peripheral nerve during repair using small gap conduit tube, Neural. Regen Res. 12 (9) (2017) 1538–1543.

[46] Y. Qian, Y. Zheng, J. Jin, X. Wu, K. Xu, M. Dai, Q. Niu, H. Zheng, X. He, J. Shen, Immunoregulation in diabetic wound repair with a photoenhanced glycyrrhizic acid hydrogel scaffold, Adv. Mater. 34 (29) (2022).

[47] J. Li, Y. Yao, Y. Wang, J. Xu, D. Zhao, M. Liu, S. Shi, Y. Lin, Modulation of the crosstalk between Schwann cells and macrophages for nerve regeneration: a therapeutic strategy based on a multifunctional tetrahedral framework nucleic acids system, Adv. Mater. 34 (46) (2022).

[48] M. Qin, X. Zhang, H. Ding, Y. Chen, W. He, Y. Wei, W. Chen, Y.K. Chan, Y. Shi, D. Huang, Y. Deng, Engineered probiotic bio-heterojunction with robust antibiofilm modality via "eating" extracellular polymeric substances for wound regeneration, Adv. Mater. 36 (35) (2024) e2402530.

[49] J. Liu, M. Qu, C. Wang, Y. Xue, H. Huang, Q. Chen, W. Sun, X. Zhou, G. Xu, X. Jiang, A dual-cross-linked hydrogel patch for promoting diabetic wound healing, Small 18 (17) (2022).

[50] G.C. Gurtner, S. Werner, Y. Barrandon, M.T. Longaker, Wound repair and regeneration, Nature 453 (7193) (2008) 314–321.

[51] K. Zha, Y. Xiong, W. Zhang, M. Tan, W. Hu, Z. Lin, P. Cheng, L. Lu, K. Cai, B. Mi, Q. Feng, Y. Zhao, G. Liu, Waste to wealth: near-infrared/pH dual-responsive copper-humic acid hydrogel films for bacteria-infected cutaneous wound healing, ACS Nano 17 (17) (2023) 17199–17216.

[52] Y. Zhao, D. Wang, T. Qian, J. Zhang, Z. Li, Q. Gong, X. Ren, Y. Zhao, Biomimetic nanozyme-decorated hydrogels with H2O2-activated oxygenation for modulating immune microenvironment in diabetic wound, ACS Nano 17 (17) (2023) 16854–16869.

[53] W.-T. Cao, F.-F. Chen, Y.-J. Zhu, Y.-G. Zhang, Y.-Y. Jiang, M.-G. Ma, F. Chen, Binary strengthening and toughening of MXene/cellulose nanofiber composite paper with nacre-inspired structure and superior electromagnetic interference shielding properties, ACS Nano 12 (5) (2018) 4583–4593.

[54] Z. Liu, T. Wang, L. Zhang, Y. Luo, J. Zhao, Y. Chen, Y. Wang, W. Cao, X. Zhao, B. Lu, F. Chen, Z. Zhou, L. Zheng, Metal–phenolic networks-reinforced extracellular matrix scaffold for bone regeneration via combining radical-scavenging and photo-responsive regulation of microenvironment, Adv. Healthcare Mater. (2024).

[55] Q. Jiang, B. Luo, Z. Wu, B. Gu, C. Xu, X. Li, X. Wang, Corn stalk/AgNPs modified chitin composite hemostatic sponge with high absorbency, rapid shape recovery and promoting wound healing ability, Chem. Eng. J. 421 (2021).